DCC regulates astroglial development essential for telencephalic morphogenesis and corpus callosum formation

Authors: Laura Morcom[1], Ilan Gobius[1], Ashley P L Marsh[2,3], Rodrigo Suárez[1,4], Jonathan WC Lim[1], Caitlin Bridges[1], Yunan Ye[1], Laura R Fenlon[1,4], Yvrick Zagar[5], Amelia M Douglass[1], Amber-Lee S Donahoo[1], Thomas Fothergill[1], Samreen Shaikh[1], Peter Kozulin[1], Timothy J Edwards[1,6], Helen M Cooper[1], IRC5 Consortium[7], Elliott H Sherr[8], Alain Chédotal[4], Richard J Leventer[3,9,10], Paul J Lockhart[2,3], & Linda J Richards[1,4]*.

Affiliations

[1]*The University of Queensland, Queensland Brain Institute, Brisbane, QLD 4072, Australia.*

[2]*Bruce Lefroy Centre for Genetic Health Research, Murdoch Children's Research Institute, Royal Children's Hospital, Parkville, VIC 3052, Australia.*

[3]*Department of Paediatrics, University of Melbourne, Parkville, VIC 3052, Australia.*

[4]*The University of Queensland, School of Biomedical Sciences, Brisbane, QLD 4072, Australia.*

[5]*Sorbonne Université, INSERM, CNRS, Institut de la Vision, 17 Rue Moreau, 75012 Paris, France.*

[6]*The University of Queensland, Faculty of Medicine, Brisbane, QLD 4072, Australia.*

[7]*Members and Affiliates of the International Research Consortium for the Corpus Callosum and Cerebral Connectivity (IRC5)*

[8]*Departments of Neurology and Pediatrics, Institute of Human Genetics and Weill Institute of Neurosciences, University of California, San Francisco, San Francisco, CA 94143, USA.*

[9]*Neuroscience Research Group, Murdoch Children's Research Institute, Parkville, VIC 3052, Australia.*

[10]*Department of Neurology, University of Melbourne, Royal Children's Hospital, Parkville, VIC 3052, Australia.*

*Corresponding author:
Professor Linda J. Richards, PhD
NHMRC Principal Research Fellow

Head, Brain Development and Disorders Laboratory,
The Queensland Brain Institute and The School of Biomedical Sciences
The University of Queensland, St Lucia, 4072, AUSTRALIA
ph: +61 7 33466355
fax: +61 7 33466301
email: richards@uq.edu.au

Current addresses: The University of Cambridge, Department of Paediatrics, Wellcome-MRC Stem Cell Institute, Cambridge, Cambridgeshire CB2 0QQ, United Kingdom (LM), The University of Queensland, Diamantina Institute, Brisbane, QLD 4102 (IG), and School of Biomedical Sciences, Brisbane, QLD 4072, Australia (SS); Departments of Child Health, Neurology, Cellular and Molecular Medicine and Program in Genetics, University of Arizona College of Medicine, Phoenix, AZ 85004 (AM), USA; Division of Endocrinology, Diabetes, and Metabolism, Department of Medicine, Beth Israel Deaconess Medical Center, Harvard Medical School, Boston, MA 02215, USA (AMD); Great Ormond Street Institute of Child Health, University College London, London, WC1E 6BT, United Kingdom (TJE); Bruker Fluorescence Microscopy, Madison, WI 53711, USA (TF).

Email addresses of other authors:
Laura Morcom: laura.morcom@uqconnect.edu.au
Ilan Gobius: ilan.gobius@gmail.com
Ashley P. L. Marsh: ashley.marsh@mcri.edu.au
Rodrigo Suárez: r.suarez@uq.edu.au
Jonathan WC Lim: j.lim5@uq.edu.au
Caitlin Bridges: caitybridges1990@gmail.com
Yunan Ye: yunan.ye@uq.edu.au
Laura R Fenlon: l.fenlon@uq.edu.au
Yvrick Zagar: yvrick.zagar@inserm.fr
Amelia M Douglass: adougla3@bidmc.harvard.edu
Amber-Lee Donahoo: amberlee.donahoo@gmail.com
Thomas Fothergill: thomas.fothergill@bruker.com
Samreen Shaikh: s.shaikh@uq.edu.au
Peter Kozulin: p.kozulin@uq.edu.au

Timothy J. Edwards: timothy.edwards2@uqconnect.edu.au
Elliott Sherr: Elliott.Sherr@ucsf.edu
Helen M. Cooper: h.cooper@uq.edu.au
IRC5: admin@irc5.org
Alain Chédotal: alain.chedotal@inserm.fr
Richard J. Leventer: richard.leventer@rch.org.au
Paul J. Lockart: paul.lockhart@mcri.edu.au

Abstract

The forebrain hemispheres are predominantly separated during embryogenesis by the interhemispheric fissure (IHF). Radial astroglia remodel the IHF to form a continuous substrate between the hemispheres for midline crossing of the corpus callosum (CC) and hippocampal commissure (HC). DCC and NTN1 are molecules that have an evolutionarily conserved function in commissural axon guidance. The CC and HC are absent in *Dcc* and *Ntn1* knockout mice, while other commissures are only partially affected, suggesting an additional aetiology in forebrain commissure formation. Here, we find that these molecules play a critical role in regulating astroglial development and IHF remodelling during CC and HC formation. Human subjects with *DCC* mutations display disrupted IHF remodelling associated with CC and HC malformations. Thus, axon guidance molecules such as DCC and NTN1 first regulate the formation of a midline substrate for dorsal commissures prior to their role in regulating axonal growth and guidance across it.

Keywords

Midline zipper glia; astrocyte morphology; agenesis of the corpus callosum; callosal axons; Deleted in colorectal cancer; NTN1, DCC mutations; telencephalic development; interhemispheric fissure remodelling

Introduction

The corpus callosum (CC) is the largest fibre tract in the human brain and is comprised of approximately 200 million axons (Paul et al., 2007; Tomasch, 1954) connecting similar regions between the left and right cerebral hemispheres (Fenlon and Richards, 2015; Fenlon et al., 2017; Suárez et al., 2018). All eutherian mammals have a CC (Suárez et al., 2014; Suárez, 2017), with malformations or complete absence (agenesis) of the CC occuring in at least 1 in 4000 human live births (Glass et al., 2008). Collectively, these genetically heterogeneous disorders are known as CC dysgenesis, and can result in a wide spectrum of neurological, developmental and cognitive deficits (Brown and Paul, 2019; Edwards et al., 2014; Paul et al., 2007).

During brain development, the callosal tract forms between the two telencephalic hemispheres through a midline region initially separated by the interhemispheric fissure (IHF; Gobius et al., 2016; Rakic and Yakovlev, 1968; Silver et al., 1982). Recently, we demonstrated that remodelling of the IHF tissue by specialised astroglial cells, known as midline zipper glia (MZG; Silver et al., 1993), is mediated by FGF8 signalling and subsequent regulation of astrogliogenesis by NFI transcription factors, and is essential to provide a permissive substrate for callosal axons to cross the telencephalic midline (Gobius et al., 2016). MZG are derived from radial glia in the telencephalic hinge, located rostral to the third ventricle. From this ventricular zone, they migrate rostro-dorsally as bipolar cells to the IHF pial surface and transition into multipolar astrocytes. This latter step facilitates their intercalation across the midline and subsequent elimination of the intervening leptomeningeal tissue that comprises the IHF. The MZG thereby fuse the medial septum in a fashion that resembles a ‘zipper’ mechanism (Gobius et al., 2016), which does not occur in naturally acallosal mammals such as monotremes and marsupials (Gobius et al., 2017). Developmental defects in IHF remodelling invariably result in callosal agenesis in mouse models and, strikingly, all 38 individuals in a human cohort with callosal agenesis also displayed aberrant retention of the IHF and an abnormal separation of the medial septum (Gobius et al., 2016). Thus, the remarkably high prevalence of midline defects in human callosal disorders suggests that there are additional determinant genes for IHF remodelling that have not yet been identified. These could include axon guidance genes, which are frequently mutated in humans (and mice) with CC abnormalities (Edwards et al., 2014).

Netrin 1 (NTN1) is a secreted ligand for the deleted in colorectal carcinoma (DCC) receptor, and these molecules function as axon guidance cues in species ranging from *Drosophila* to mammals (Chan et al., 1996; de la Torre et al., 1997; Fazeli et al., 1997; Hedgecock et al., 1990; Keino-Masu et al., 1996; Kolodziej et al., 1996; Serafini et al., 1996). Indeed, NTN1-DCC signalling attracts pioneering callosal axons towards the midline and attenuates chemorepulsive signaling in neocortical callosal axons *ex vivo* to facilitate crossing the midline (Fothergill et al., 2014). Heterozygous and homozygous *DCC* pathogenic variants also result in human callosal dysgenesis at high frequency (Jamuar et al., 2017; Marsh et al., 2018; Marsh et al., 2017) with an estimated incidence of 1 in 14 in unrelated individuals with callosal dysgenesis (Marsh et al., 2017), and *Ntn1* and *Dcc* mouse mutants do not form a CC (Fazeli et al., 1997; Finger et al., 2002; Fothergill et al., 2014; Serafini et al., 1996). Instead of crossing the midline, callosal axons in *Ntn1* and *Dcc* mutant mice form ipsilateral “Probst” bundles that run parallel to the midline (Fazeli et al., 1997; Finger et al., 2002; Fothergill et al., 2014; Ren et al., 2007; Serafini et al., 1996). Together, these results have led to the conclusion that NTN1 and DCC act primarily as axon guidance genes during callosal formation. However, in *Ntn1* and *Dcc* mutant mice, only the CC and hippocampal commissure (HC) are completely absent, while other axon tracts remain intact or are mildly affected (Fazeli et al., 1997; Serafini et al., 1996; Yung et al., 2015), indicating that additional processes might affect the development of the CC and HC in these mice. Moreover, elimination of the leptomeninges, which normally occurs during IHF remodelling (Gobius et al., 2016), is severely disrupted in *Ntn1* mutant mice (Hakanen and Salminen, 2015), further suggesting that NTN1 and its receptor, DCC, may play a hitherto unidentified role in IHF tissue remodelling.

Here, we identify a distinct and developmentally earlier role for NTN1 and DCC signalling during CC formation, involving the regulation of MZG development and subsequent IHF remodelling. We find that IHF remodelling is impaired in both *Ntn1* and *Dcc* mouse mutants, as well as in humans with *DCC* pathogenic variants that also display agenesis of the CC and HC. Moreover, in contrast to the wildtype receptor, these human pathogenic variants of *DCC* are unable to regulate cell morphology. Furthermore, we find that defects in astroglial morphology and migration to the IHF in *Ntn1* and *Dcc* mutant mice prevent MZG intercalation and, therefore, IHF remodelling and midline crossing of commissural axons. Taken

together, our findings indicate that pathogenic variants in *NTN1* and *DCC* are most likely to affect human CC and HC development through misregulation of astroglial shape, motility and function during IHF remodelling.

Results

Dcc signalling is required for IHF remodelling and subsequent CC and HC formation

To re-investigate how *Dcc* and *Ntn1* regulate callosal formation, we first analysed the relationship between the IHF and callosal axon growth during midline development in horizontal sections of *Ntn1* and *Dcc* mutant mice. These mouse mutants include *Dcc* knockout, Dcc^{kanga} mice, which express a truncated DCC receptor that lacks the P3 intracellular signalling domain, and *Ntn1-lacZ* mutant mice, which express reduced levels of NTN1 protein that subsequently becomes sequestered in intracellular organelles (Fazeli et al., 1997; Finger et al., 2002; Fothergill et al., 2014; Serafini et al., 1996). Immunohistochemistry was performed following commissure formation at embryonic day (E)17 against the axonal marker Gap43 together with pan-Laminin, which labels both leptomeningeal fibroblasts and the basement membrane surrounding the IHF (Figure 1A). This revealed that commissural axons in *Dcc* knockout, Dcc^{kanga}, and *Ntn1-lacZ* mice remain within the ipsilateral hemisphere and do not form a CC or HC, consistent with previous reports (Fazeli et al., 1997; Finger et al., 2002; Fothergill et al., 2014; Ren et al., 2007; Serafini et al., 1996). We further identified that IHF remodelling had not occurred in *Dcc* knockout, Dcc^{kanga}, and *Ntn1-lacZ* mice, evidenced by complete retention of the IHF, which separated the majority of the telencephalic midline (Figure 1A). This likely prevented formation of the HC in addition to the CC (Figure 1A). The extent of IHF retention, measured as the ratio of IHF length to total midline length, is significantly larger in *Dcc* and *Ntn1* mutants compared to their wildtype littermates (Supplementary File 1; Figure 1A and 1B), but did not differ between mutants (Supplementary File 1; Figure 1A and 1B). This suggests that NTN1 and DCC may interact or act in a similar manner to regulate IHF remodelling prior to commissural axon crossing, and that the P3 intracellular domain of DCC is crucial for this function. The brain phenotype of adult *Dcc* knockout and *Ntn1-lacZ* mice was unable to be investigated as these animals die shortly after birth (Fazeli et al., 1997; Finger et al., 2002; Serafini et al., 1996). However, immunohistochemistry for the axonal marker Neurofilament in adult Dcc^{kanga} mice

revealed that the retention of the IHF and absence of the CC and HC persists into adulthood (Supplementary File 1; Figures 1B and Figure 1-figure supplement 1), resembling human congenital callosal agenesis (Edwards et al., 2014; Gobius et al., 2016).

We previously reported that humans carrying *DCC* pathogenic variants develop dysgenesis of the CC with incomplete penetrance (Marsh et al., 2017). T1-weighted MRI of four individuals from two unrelated families carrying missense pathogenic variants in *DCC* (p.Val793Gly affecting fibronectin type III-like domain 4 of *DCC* and p.Met1217Val; p.Ala1250Thr affecting the cytoplasmic domain of *DCC*; Figure 8A; Marsh et al., 2017), revealed in all cases that the complete absence of the CC was associated with aberrant retention of the IHF and an unfused septum (Figure 1C). Importantly, these individuals were also previously reported to lack a HC (Marsh et al., 2017), suggesting a defect in IHF remodelling may also impact HC development. Since IHF remodelling is required for subsequent callosal axon crossing (Gobius et al., 2016), these results collectively suggest that the underlying cause of callosal agenesis in *Ntn1* and *Dcc* mutant mice and in humans with *DCC* mutations is a failure of IHF remodelling.

DCC and NTN1 are expressed by MZG cells throughout interhemispheric remodelling

We previously demonstrated that DCC is expressed on axons of the CC, HC and the fornix during midline development, while NTN1 is expressed at the telencephalic midline, within the indusium griseum and the septum but not within callosal axons themselves (Fothergill et al., 2014; Shu et al., 2000). Since our analysis of *Ntn1* and *Dcc* mutant mice revealed that these genes are necessary for IHF remodelling, we then investigated whether they are expressed by the MZG, which mediate IHF remodelling (Gobius et al., 2016). MZG arise in the telencephalic hinge, a region in the septal midline caudal to the IHF and rostral to the third ventricle. Radial glia within the telencephalic hinge are attached to both the third ventricle and the IHF and mature into MZG as they undergo somal translocation to the IHF between E12 and E16 in mice (Gobius et al., 2016). Fluorescent *in situ* hybridization for *Dcc* and *Ntn1* transcripts, combined with immunohistochemistry for the MZG marker Glast (Gobius et al., 2016), revealed *Dcc* and *Ntn1* expression in radial MZG progenitor cells within the telencephalic hinge at E12 and E15 (Figure 2B-2D, 2F and 2H; Figure 2-figure

supplement 1H-J), and in MZG migrating to the IHF at E15 (Figure 2F and 2H). Furthermore, *Dcc* was expressed in Glast-positive radial glia within the septum but not in the neocortex (Figure 2-figure supplement 1A-C). DCC protein can be identified on Glast-positive processes of radial glia attached to the IHF (Figure 2G), which are adjacent to Gap43-positive axons traversing the midline region that also express DCC (Figure 2-figure supplement 1E). Following IHF remodelling at E17, mature Gfap-positive/Sox9-positive multipolar MZG cells (Gobius et al., 2016; Sun et al., 2017) and Glast-positive MZG cells within the telencephalic hinge continue to express DCC (Figure 2J-2L). A comparison of DCC immunohistochemistry in wildtype and *Dcc* knockout mice confirmed that the antibody specifically recognised DCC protein within both commissural axons and MZG cells (Figure 2-figure supplement 1K). Importantly, we did not observe specific staining for either *Dcc or Ntn1* mRNA within the IHF (including the leptomeninges) at any stage analysed (Figures 2 and S2).

Since NTN1 is a secreted cue (Kennedy et al., 1994; Sun et al., 2011), we investigated which cells express NTN1, and where secreted NTN1 may be deposited, by comparing patterns of immunohistochemistry for β-galactosidase (β-gal) and NTN1 antibodies in heterozygous and homozygous *Ntn1-lacZ* mutants, in which NTN1 is fused to a β-gal and trapped in intracellular compartments (Serafini et al., 1996). NTN1/βgal-positive puncta were enriched in Glast-positive MZG cells in *Ntn1-lacZ* mice (Figure 2I). Furthermore, we identified NTN1 protein on the IHF basement membrane (Figures 2I and S2G), on growing commissural axons (Figure 2-figure supplement 1G), and on MZG membranes in control heterozygotes, but not in *Ntn1-lacZ* homozygous mutant mice (Figure 2I). Therefore, MZG cells produce and secrete NTN1 that becomes deposited on the basement membrane of the IHF, on commissural axons, and on MZG cell processes in the region of initial IHF remodelling (Figure 2E). Collectively, our results demonstrate that both *Ntn1* and *Dcc* are expressed by MZG, and suggest that autocrine NTN1-DCC signalling may regulate MZG development and subsequent IHF remodelling.

Dcc signalling regulates MZG cell morphology and process organisation prior to IHF remodelling

Two key steps in IHF remodelling are the somal translocation of radial MZG progenitors to the IHF, and their subsequent transition into multipolar MZG cells that intercalate across the midline (Gobius et al., 2016). As both NTN1 and DCC are expressed by MZG, we next asked whether these molecules regulate MZG development. Immunohistochemistry for Nestin and Glast, which are markers of radial MZG, revealed distinct differences in MZG development in *Dcc*^{kanga} mice from E14 onward, but not in radial MZG progenitors at E13 (Figure 3-4 A). In wildtype mice, the endfeet and cell bodies of radial Glast-positive MZG cells are evenly distributed along the medial septum and adjacent to the pial surface of the IHF (Figures 3B, 3D, 4A and 4C). However, in *Dcc*^{kanga} mutants, radial MZG accumulate at the base of the IHF (Figure 3A-D). Furthermore, long radial Nestin-positive MZG processes extending from the ventricular zone to the rostral-most pial surface of the IHF are noticeably absent from *Dcc*^{kanga} mutants, and instead, Nestin-positive *Dcc*^{kanga} processes cluster close to the rostral IHF pial surface and appear disorganised (Figures 3A, 3C, 3C', 3E and 3-figure supplement 1B-D). These abnormalities were further quantified as a significant increase in fluorescence intensity of Glast staining within the base of the IHF, and a concomitant decrease in the region 150-200 µm distant from the IHF base in *Dcc*^{kanga} mutants, compared to their wildtype littermates at E14 (Supplementary File 1; Figure 3B, 3B' and 3G). Just prior to IHF remodelling at E15, there was an overall decrease in Glast-positive radial MZG processes in *Dcc*^{kanga} mutants (Figure 3C, 3H and Supplementary File 1). While there was no difference in fluorescence intensity of Glast-positive radial MZG processes one day later at E16, *Dcc*^{kanga} MZG processes continued to display irregular morphology and failed to intercalate across the IHF (Figure 3E, 3F, 3I and Supplementary File 1). Interestingly, we identified a similar defect in the distribution of Glast-positive MZG processes in *Ntn1-lacZ* mutant mice at E15 (Figure 3K). These results suggest that both DCC and NTN1 are required for the correct morphology and distribution of MZG processes prior to IHF remodelling. Moreover, abnormal morphology and increased abundance of GLAST-positive and NESTIN-positive radial fibers of the dorsal glial population, known as the glial wedge, was also evident in E15 *Dcc*^{kanga} mice (Figure 3C-D), suggesting DCC regulates the morphology and distribution of at least 2 midline glial populations prior to CC development.

To further characterise the defect in MZG cell distribution in *Dcc*^{kanga} mice, we then measured the maximum rostro-caudal extent to which MZG occupy the IHF pial surface, and normalised this value to the total midline length from E14-E16 (Figure 3A-F and 3J). The distribution of Nestin-positive and Glast-positive MZG along the IHF was significantly decreased at both E14 and E15 in *Dcc*^{kanga} mice compared to their wildtype littermates (Figure 3A-D, 3J and Supplementary File 1). The attachment of MZG processes to the IHF pial surface is therefore specifically reduced in the rostral region of the IHF prior to IHF remodelling in *Dcc*^{kanga} mice. This may impact the directed somal translocation of *Dcc*^{kanga} MZG cell bodies and their subsequent distribution along the IHF surface prior to IHF remodelling.

Next, we further investigated whether the aberrant organisation of radial glial processes along the IHF in *Dcc*^{kanga} mice was due to a loss of endfoot adhesion to the IHF pial surface. There was no difference in fluorescence intensity of Nestin-positive MZG processes within 5 µm adjacent to the IHF surface between *Dcc*^{kanga} and wildtype mice, suggesting comparable attachment of radial glial endfeet to the IHF in both strains (Supplementary File 1, Figure 3-figure supplement 1E and G). This was further evidenced by the normal localisation of α- and β-dystroglycan at the pial IHF surface in *Dcc*^{kanga} mice, where these molecules form crucial adhesions between radial glial endfeet and the extracellular matrix (Myshrall et al., 2012; Supplementary File 1; Figure 3-figure supplement 1-D). Moreover, molecules that normally maintain the bipolar morphology of radial glia, such as β-catenin and N-cadherin, were also expressed normally within *Dcc*^{kanga} Nestin-positive radial glia, but adenomatous polyposis coli (APC) was instead significantly reduced in *Dcc*^{kanga} Nestin-positive radial glial endfeet (Supplementary File 1, Figure 3-figure supplement 1D and 3-figure supplement 1E; Yokota et al., 2009). APC regulates the growth and extension of basal radial glial processes and cell polarity of radial glia and migrating astrocytes (Etienne-Manneville and Hall, 2003; Yokota et al., 2009). Thus, reduced localisation of APC within *Dcc*^{kanga} radial glial basal endfeet may indicate perturbed regulation of cell process growth and/or cell polarity. Therefore, *Dcc*^{kanga} Nestin-positive radial glia display reduced elongation and reduced occupation of the pial IHF surface compared to wildtype radial progenitors of MZG. Collectively, these results suggest that DCC is not required for radial MZG to adhere to the IHF, but instead regulates the morphology and organisation of radial MZG processes along the pial IHF surface prior to IHF remodelling.

Dcc signalling regulates MZG somal translocation to the IHF prior to IHF remodelling

To determine if the aberrant morphology and organisation of radial glial processes observed in *Dcc*^{kanga} mice affects the subsequent distribution of translocated MZG cell bodies at the IHF surface, immunohistochemistry for glial markers Sox9 and Glast was performed in E14-E16 *Dcc*^{kanga} mice. Wildtype MZG undergo substantial somal translocation to the IHF between E14 and E15 (Gobius et al., 2016; Supplementary File 1, Figure 4A, 4C and 4G). In contrast, *Dcc*^{kanga} mice showed reduced somal translocation to the IHF (Supplementary File 1; Figure 4A, 4C and 4G), with significantly fewer MZG cells at the IHF pial surface by E15 in *Dcc*^{kanga} compared to wildtype mice (Supplementary File 1; Figure 4B and 4G). When binned along the rostro-caudal axis, we found a significant reduction in the number of cell bodies reaching the rostral IHF pial surface in E15 *Dcc*^{kanga} mice (200-250 µm; Supplementary File 1 and Figure 4C-D). Since MZG progenitors somal translocate toward their basal process attached to the IHF (Gobius et al., 2016), our results suggest that the lack of radial MZG processes occupying the rostral E14 IHF surface in *Dcc*^{kanga} mice results in a decrease of MZG cell bodies present in the corresponding region one day later. There was, however, a significant increase in MZG cell bodies present at the IHF pial surface between E15 and E16 in *Dcc*^{kanga} mice (Supplementary File 1, Figure 4C, 4E and 4G). This suggests that MZG migration towards the IHF is delayed but does eventually occur in *Dcc*^{kanga} mice, albeit after IHF remodelling would normally have been initiated. *Dcc*^{kanga} MZG remain adjacent to the unremodelled IHF at E16 in contrast to wildtype MZG, which are scattered along the midline where IHF remodelling has occurred and continue to expand their domain rostral and dorsal for further IHF remodelling (Gobius et al., 2016). Furthermore, despite DCC having been previously implicated in regulating cell proliferation and cell death (Arakawa, 2004; Llambi et al., 2001; Mehlen et al., 1998), cell birth-dating, differentiation and apoptosis experiments did not reveal any significant differences between the MZG of *Dcc*^{kanga} and wildtype mice (Supplementary File 1 and Figure 4-figure supplement 1). Taken together, these results suggest that the irregular morphology and distribution of radial *Dcc*^{kanga} MZG processes is associated with delayed somal translocation of MZG to the IHF surface, and may prevent the initiation of IHF remodelling.

Radial glia in the corticoseptal boundary detach from the pial surface and cluster their processes to form a triangular group of cells known as the glial wedge, while other radial glia in this region translocate their soma to the IHF (similar to MZG cells), where they subsequently form the indusium griseum glia (Shu and Richards, 2001; Smith et al., 2006). We investigated whether DCC also regulates the development of these glial populations, which were observed to be abnormal at E15 (Figure 3C-D) and secrete axon guidance molecules during CC formation (reviewed in Donahoo and Richards, 2009; Gobius and Richards, 2011; Morcom et al., 2016). In *Dcc*^{kanga} and *Dcc* knockout mice, the glial wedge was malformed and there was a major reduction in somal translocation of Sox9-positive indusium griseum glia to the IHF surface, which subsequently prevented formation of this glial guidepost cell population (Supplementary File 1 and Figure 4-figure supplement 1G-I). Thus, DCC may play a more general role in regulating the morphological maturation and migration of multiple radial astroglial populations in the developing midline, which are critical for CC formation.

DCC signalling regulates MZG cell morphology and spatial distribution during IHF remodelling

We previously demonstrated that MZG differentiation is controlled by molecular signaling initiated by the morphogen FGF8 via the Mitogen activated protein kinase (MAPK) pathway to NFI transcription factors A and B (Gobius et al., 2016). Members of this signaling pathway (*Fgf8*, NFIA, NFIB, and p-ERK1/2) were expressed normally in *Dcc*^{kanga} MZG compared to MZG in their wildtype littermates at E15 (Figure 5-figure supplement 1B, S5D-F and Supplementary File 1). Further, *Dcc*^{kanga} MZG continue to express *Mmp2* mRNA (Figure 5-figure supplement 1C, D and Supplementary File 1), which we previously demonstrated to be expressed during MZG-mediated degradation of the IHF during remodelling (Gobius et al., 2016).

Next, we investigated the distribution and maturation of MZG in *Ntn1* and *Dcc* mutant mice at E16 and 17, when wildtype MZG normally differentiate into multipolar astrocytes during IHF remodelling (Gobius et al., 2016). Immunohistochemistry for Nestin, Glast (Figures 3F, 3J) and Gfap (Figure 5A) demonstrated that *Dcc*^{kanga}, *Dcc* knockout and *Ntn1-lacZ* MZG remain attached to the caudal IHF pial surface and have not intercalated at stages equivalent to when wildtype MZG have infiltrated and remodelled the IHF (Figures 3F, 3J, 5A and Supplementary File 1). DCC-deficient

MZG expressed GFAP at comparable levels to wildtype MZG at E17, and demonstrated no precocious expression of GFAP at E15, similar to wildtype MZG (Figure 5A-B, Figure 5-figure supplement 1A and Supplementary File 1). Therefore, DCC-deficient MZG do not mature precociously prior to migration and IHF remodelling, or fail to differentiate during callosal development. However, *Ntn1-lacZ*, *Dcc*^{kanga} and *Dcc* knockout mice demonstrate a significant reduction of GFAP-positive glia at E17 in the region where the CC normally forms in wildtype mice (i.e., > 450 µm from the third ventricle; Figure 5A-C and Supplementary File 1). Instead, MZG in these mutants remain close to the third ventricle and the majority fail to migrate. To quantify this, we normalised the level of GFAP between sections and calculated a rostro-caudal ratio of this fluorescence. We observed a significant reduction in the rostro-caudal ratio of GFAP fluorescence in *Ntn1-lacZ*, *Dcc*^{kanga} and *Dcc* knockout mice compared to controls (Figure 5A-D and Supplementary File 1). Since progressive migration and intercalation of MZG is required for IHF remodelling (Gobius et al., 2016), these results indicate that *Ntn1* and *Dcc* affect IHF remodelling by regulating the morphology and spatial organisation of both radial MZG progenitors and mature MZG, and therefore their ability to intercalate across the IHF, but not their proliferation and adhesion to the pial IHF surface.

Variable DCC knockdown during midline development causes a spectrum of callosal phenotypes.

The current and previous results from our laboratory indicate at least two distinct roles for NTN1 and DCC during CC formation: first, they act on astroglia to facilitate remodelling of the IHF, and second, they regulate the pathfinding of callosal axons to the telencephalic midline (Fothergill et al., 2014). To investigate these roles further, we aimed to disrupt DCC expression specifically within the progenitors of callosal neurons, sparing expression within MZG. We designed two *Dcc*-targeted CRISPR/CAS9 constructs (*Dcc*-CRISPR) and acquired a *Dcc*-targeted shRNA (*Dcc*-shRNA; Zhang et al., 2018) for targeted in utero electroporation into the E13 cingulate cortex in wildtype and *Dcc*^{kanga} mice and successfully labelled callosal axons that reach the contralateral hemisphere by E18 (Figure 6-figure supplement 1A). We observed no phenotype in all experimental cases (Figure 6-figure supplement 1A), and instead found these techniques failed to reduce DCC expression sufficiently; the only significant reduction in DCC protein was observed in

heterozygous *Dcc*^{kanga} mice electroporated with *Dcc*-shRNA (average DCC expression reduced to 93.06% compared to the non-electroporated hemisphere; Figure 6-figure supplement 1A-C and Supplementary File 1). In order to knockout DCC more robustly in the cortex, we crossed *Dcc*$^{flox/flox}$ mice (Krimpenfort et al., 2012) with mice carrying *Emx1*^{iCre} (Kessaris et al., 2006), and the *tdTomato*$^{flox\_stop}$ reporter allele (Madisen et al., 2010).

At birth, we observed a spectrum of callosal phenotypes in *Dcc* cKO mice, including complete callosal absence (4/12 mice), partial CC absence (5/12 mice), and a normal CC that was comparable to control mice, which do not express *Emx1*^{iCre} (3/12 mice) based on rostral-caudal CC length across ventral, middle and dorsal horizontal sections (Figure 6A and 6F). Moreover, the HC was significantly reduced in the majority of animals and was absent in one *Dcc* cKO mouse (Figure 6A, 6H and Supplementary File 1). Unexpectedly, we found the IHF was significantly retained across *Dcc* cKO mice, indicating that IHF remodelling had not been completed (Figure 6A, 6D-E, and Supplementary File 1). The severity of callosal agenesis and HC dysgenesis was significantly correlated with the extent to which the IHF had been remodelled (Figure 6A, 6J, 6K, Figure 6-figure supplement 1D-G and Supplementary File 1). Complete callosal agenesis *Dcc* cKO mice demonstrated the most severe retention of the IHF, encompassing the majority of the telencephalic midline, while partial callosal agenesis and even full CC *Dcc* cKO mice demonstrated a retention of the rostral IHF (Figure 6A, 6E and Supplementary File 1). Moreover, in partial callosal agenesis and full CC *Dcc* cKO mice that demonstrated partial retention of the rostral IHF, callosal axons often crossed the midline more caudal in a region where the IHF had been remodelled compared to control mice (see corpus callosum remnant or CCR in Figure 6A). This suggests that in the absence of their normal substrate, callosal axons are able to adapt and cross the midline in a region where the substrate is available. These results were reflected by a significant increase in the rostro-caudal depth of the partial or full CC in *Dcc* cKO mice (Figure 6A, 6G and Supplementary File 1). In *Dcc* cKO mice with complete callosal agenesis, callosal axons were unable to cross the midline and accumulated adjacent to the IHF that had not been remodelled (red arrowheads in Figure 6A), similar to *Dcc*^{kanga} and *Dcc* knockout mice. These results demonstrate that DCC regulates the extent of IHF remodelling throughout the telencephalic midline. The retention of the IHF in these mice was unexpected; we had instead expected that reduced DCC

expression in the cortex would cause callosal axon misguidance with normal formation of an interhemispheric substrate. Instead, our results suggest that DCC primarily regulates the formation of the interhemispheric substrate to determine CC size in mice.

We next explored whether loss of DCC expression within callosal axons might cause prior callosal axon misguidance that could indirectly impact IHF remodelling. We found that DCC expression was significantly reduced in the cingulate cortex and adjacent intermediate zone in the majority of P0 *Dcc* cKO mice (mean expression reduced to 80.4% and 62.9% respectively; Figure 6A, 6I and Supplementary File 1), and within E15 *Dcc* cKO mice (mean DCC expression in the cingulate cortex reduced to 76.6% in *Dcc* cKO; Figure 6L, 6O and Supplementary File 1), as expected. Surprisingly, we found that TDTOMATO-positive/GAP43-positive axons, which had reduced DCC expression, approached the interhemispheric midline in *Dcc* cKO mice, similar to their cre-negative littermates (Figure 6M-N, 6P and Supplementary File 1). This suggests that axons with reduced, but not entirely eliminated DCC expression, approach the midline adjacent to the IHF in a timely and spatially appropriate manner, and are unable to cross the midline in regions where the IHF is not remodelled in *Dcc* cKO mice.

Next, we investigated the recombination pattern and development of MZG in *Dcc* cKO mice. Cre activity, as measured by TDTOMATO expression, was widespread in cells throughout the telencephalic midline, including septal cells and HC axons, resulting in reduced DCC expression in multiple cell types (Figure 6B). Mean DCC expression within the telencephalic hinge was comparable between *Dcc* cKO mice and their cre littermates (Figure 6L, 6O and Supplementary File 1), but we also observed TDTOMATO-positive/GLAST-positive MZG cell bodies within the telencephalic hinge, and at the IHF surface in *Dcc* cKO mice (Figure 6Q-R and Supplementary File 1). This suggests the potential for *Dcc* knockdown in a subset of MZG cells within *Dcc* cKO mice, which may fail to intercalate across the IHF, possibly causing the IHF remodelling defect observed in P0 *Dcc* cKO mice. However, unlike Dcc^{kanga} mice, we were unable to find a significant population difference in the distribution of GLAST-positive MZG between *Dcc* cKO mice and their cre-negative littermates, at the level of DCC knockdown observed in this model (Figure 6-figure supplement 1H-I and Supplementary File 1). Thus, the variable callosal and IHF remodelling phenotypes observed in *Dcc* cKO mice likely arise from

varying degrees of DCC knockdown in these models due to the mosaic expression of *Emx1*^{iCre} within MZG. In order to further explore the role of DCC and the impact of human *DCC* mutations on the behavior of astroglia, we next investigated the function of human *DCC* mutations using in vitro assays.

NTN1-DCC signalling promotes cytoskeletal remodelling of astroglia and neural progenitors

Our results suggest that NTN1 and DCC may have important functions in the morphological development of radial glia more broadly. We established *in vitro* assays to test the function of NTN1-DCC signalling and DCC mutant receptors in regulating the morphology of astroglial-like cells. Such assays can also be used to examine human variants of DCC pathogenic mutations (see next section). To develop these assays, we employed N2A neuroblast cells, which display neural progenitor properties (Augusti-Tocco and Sato., 1969; Shea et al., 1985), as well as U251 glioma cells, which express astroglial markers and display invasive capacity (Zhang et al., 2013) similar to MZG cells. Importantly, endogenous DCC has previously been demonstrated to render several glioma cell lines migratory in response to a gradient of NTN1 as a chemoattractant (Jarjour et al., 2011). Both cell lines were transfected with either full-length DCC fused to a TDTOMATO reporter (pCAG-DCC:TDTOMATO) to express wildtype DCC, or a membrane-targeted TDTOMATO reporter (pCAG-H2B-GFP-2A-Myr-TDTOMATO) as a control and stimulated with NTN1. Moreover, we transfected U251 cells with a DCC^{kanga} construct (pCAG-DCC^{kanga}:TDTOMATO), to test whether the P3 domain was critical for NTN1-DCC signalling effects on cell morphology.

Expression of DCC:TDTOMATO in U251 cells in the absence of ligand (vehicle alone) promoted cell spreading and elongation, reflected by a significant increase in average cell area and cell perimeter, and a significant decrease in cell circularity compared to control (Supplementary File 1 and Figure 7A-F). This effect was not observed following expression of the DCC^{kanga} construct alone (Supplementary File 1 and Figure 7A-F), suggesting that the P3 domain of DCC is critical for inducing changes in glial cell shape. We further confirmed that these morphological changes were due to the presence of the coding region of wildtype DCC, by comparing to cells transfected with plasmids where DCC had been excised and only the TDTOMATO remained (pCAG-TDTOMATO; Supplementary File 1 and

Figure 7-figure supplement 1A and Figure 6-figure supplement 17B). A similar effect was observed following DCC overexpression in N2A cells, which also registered a significant increase in average cell area and cell perimeter, and decrease in cell circularity, compared to controls (Supplementary File 1, Figure 7G-I, and Figure 7-figure supplement 1G and H), further indicating similar effects on cell morphology in glial and neural progenitor lineages. Interestingly, application of NTN1 did not affect cell shape following DCC expression in either cell line (Supplementary File 1 and Figure 7A-F), suggesting that endogenous NTN1, which is known to be expressed by U251 cells (Chen et al., 2017), may be sufficient for activation of DCC:TDTOMATO receptors, or that NTN1 is not required for this effect. To investigate this, we examined NTN1 expression in these cell lines using western blot analysis. We confirmed that both our cell lines expressed NTN1 endogenously, and that transfection of DCC increased DCC levels but did not affect NTN1 expression (Figure 7-figure supplement 1J). No endogenous DCC was detected by western blot in either cell line (Figure 7-figure supplement 1J). Thus, addition of DCC induced cytoskeletal rearrangements in both N2A and U251 cells, which may involve autocrine NTN1 signalling. Typical features of DCC-expressing cells with or without bath application of NTN1 included actin-rich regions resembling filopodia, lamellipodia, and membrane ruffling in U251 cells, while only filopodia were highly abundant in DCC:TDTOMATO-expressing N2A cells; all of these features were rarely observed in control cells from both cell lines (Figure 7A, G). No difference in cleaved-caspase 3-mediated cell apoptosis was observed following DCC expression in either cell line (Figure 7-figure supplement 1I). This suggests that DCC signalling does not mediate programmed cell death but rather promotes remodelling of the actin cytoskeleton in glioma and neuroblast cells in a similar manner to neurons and oligodendrocytes (Rajasekharan et al., 2009; Shekarabi and Kennedy, 2002).

Humans with agenesis of the CC carry loss-of-function pathogenic variants in *DCC* that are unable to modulate cell shape

Having established that DCC signalling rearranges the cytoskeleton of astroglial-like cells, and that the P3 domain of DCC is crucial for this function, we next investigated whether *DCC* mutant receptors from humans with dysgenesis of the CC affected this function. Site directed mutagenesis was performed to introduce missense mutations into the pCAG-DCC:TDTOMATO expression vector in order to model mutated *DCC*

receptors found in six families with previously reported cases of complete or partial agenesis of the CC (p.Met743Leu, p.Val754Met, p.Ala893Thr, p.Val793Gly, p.Gly805Glu, p.Met1217Val;p.Ala1250Thr; Marsh et al., 2017; Marsh et al., 2018; Figure 8A and Figure 6-figure supplement 1C). We further included two artificial mutant receptors that were previously shown to perturb NTN1 binding and chemoattraction (p.Val848Arg, p.His857Ala; Finci et al., 2014). First, these mutants were transfected into HEK293T and COS-7 cells that do not endogenously express DCC (Chen et al., 2013; Shekarabi and Kennedy, 2002). Immunoblotting and immunohistochemistry performed without cell permeabilisation revealed that all mutant DCC receptors were appropriately expressed and localised to the cell membrane (Gad et al., 2000; Figure 7-figure supplement 1E). Using a previously established *in vitro* binding assay (Müller and Soares, 2006; Zelina et al., 2014), we discovered that DCC mutant proteins with altered residues located at the NTN1 binding interface (p.V793G and p.G805E) were unable to bind NTN1 (Figure 8B), while all other receptors with altered residues lying outside of the NTN1 binding interface still bound NTN1 (p.M743L, p.V754M, p.A893T and p.M1217;A1250T; Figure 8B). Surprisingly, all eight mutant *DCC* receptors were unable to modulate cell morphology in the presence of NTN1 (Figure 8C-E; Supplementary File 1). Collectively, our results suggest a model whereby mutations that affect the ability for DCC to regulate cell shape (Figure 8F), are likely to cause callosal agenesis through perturbed MZG migration and IHF remodelling.

Discussion

Genes that encode axon guidance molecules frequently cause callosal dysgenesis when knocked out in mice (Edwards et al., 2014). This has led to the prevalent view that callosal dysgenesis in these mice might be primarily to due defects in callosal axon guidance towards and across the midline. Here, we identified a novel function for the classical axon guidance genes NTN1 and DCC in regulating the morphology of midline astroglia for IHF remodelling prior to CC and HC formation. Importantly, normal astroglial development and IHF remodelling are critical processes that precede and are necessary for subsequent CC axon guidance across the interhemispheric midline (Gobius et al., 2016). We find that defects in IHF remodelling are consistently associated with dysgenesis of the CC and HC in mice and humans with pathogenic variants in *Ntn1* or *Dcc*.

Our *in vitro* assays and analysis of mouse and human cell morphology indicate that the cytoskeletal remodelling function of NTN1-DCC signalling is likely to be crucial for MZG development, IHF remodelling, and subsequent CC formation. The timely differentiation and appropriate distribution of MZG cells at the IHF surface is required for their intercalation and IHF remodelling function (Gobius et al., 2016). Our data suggest a model whereby failed IHF remodelling associated with mutations in *Ntn1* and *Dcc* occurs due to delayed astroglial migration to the IHF as a consequence of perturbed process extension and organisation of MZG precursors. Notably, no medial extension of MZG processes across the basement membrane or perforations in the IHF to allow glia from each hemisphere to interact and intercalate were observed in *Ntn1* or *Dcc* mutant mice at any developmental stage examined. This suggests that NTN1-DCC signalling might also be required for MZG intercalation and removal of the intervening leptomeninges. The DCC homologue UNC-40 is known to facilitate formation of a polarised actin-rich cell protrusion in the *Caenorhabditis elegans* anchor cell, which breaches the basement membrane rich in UNC-6 (NTN1 homolog), enabling the cell to invade the vulval epithelium (Hagedorn et al., 2013; Ziel et al., 2009). DCC may perform a similar function in MZG by engaging secreted NTN1, which we found to be localised at the IHF basement membrane in agreement with the localisation of radial-glial-derived NTN1 in the spinal cord (Varadarjan et al., 2017), and preferentially polarising actin remodelling and process extension toward the IHF during MZG intercalation. Moreover, callosal axons that also rely on DCC-mediated cytoskeletal remodelling for growth and guidance, may non-cell-autonomously influence the final stages of MZG development via a secreted cue or contact-dependent mechanism. Further dissecting this would ideally involve even greater precision in complete and cell-type specific knockout of DCC and NTN1, since knockdown in a subset of cells or merely lowering the expression level was insufficient to induce a consistent phenotype.

Notably, we find that the P3 domain-dependent functions of DCC may be required for astroglial development and IHF remodelling. These functions include receptor dimerisation, interaction with the co-receptor ROBO1, or interaction with effectors FAK, MYO10, and TUBB3 (Fothergill et al., 2014; Li et al., 2004; Qu et al., 2013; Stein and Tessier-Lavigne, 2001; Wei et al., 2011; Xu et al., 2018). Accordingly, mice deficient in *Robo1, Fak* and *Tubb3*, as well as their signaling effectors *Cdc42, Fyn*, *Enah* and *Mena,* which normally act downstream of DCC to

regulate the cell cytoskeleton, all display dysgenesis of the CC (Andrews et al., 2006; Beggs et al., 2003; Goto et al., 2008; Menzies et al., 2004; Tischfield et al., 2010; Yokota et al., 2010). Similarly, astroglial cells remodel their cytoskeleton to transition from a bipolar to multipolar morphology, and this process is known to involve the intracellular DCC effectors CDC42, RAC1, RHOA, N-WASP and EZRIN (Abe and Misawa, 2003; Antoine-Bertrand et al., 2011; Derouiche and Frotscher, 2001; Lavialle et al., 2011; Murk et al., 2013; Racchetti et al., 2012; Shekarabi et al., 2005; Zeug et al., 2018). Whether these molecules serve as downstream effectors of DCC to influence astroglial development and IHF remodelling during CC formation is an interesting question for future research.

In addition to NTN1 and DCC, as shown here, mice lacking the axon guidance molecules ENAH, SLIT2, SLIT3, and RTN4R have previously been reported to have incomplete IHF remodelling and disrupted midline glial development associated with callosal dysgenesis (Menzies et al., 2004; Unni et al., 2012; Yoo et al., 2017). Taken together, those studies and ours suggest that other axon guidance genes may play similar roles in astroglial development and IHF remodelling during CC formation. Additional candidate axon guidance molecules that may regulate IHF remodelling include EPHB1, EFNB3, GAP43, HS6ST1, HS2ST1, ROBO1 and VASP, since mouse mutants lacking these molecules display disrupted midline glial development and callosal dysgenesis (Andrews et al., 2006; Conway et al., 2011; Mendes et al., 2006; Menzies et al., 2004; Shen et al., 2004; Unni et al., 2012). Additional molecules of interest are EFNB1, EFNB3, EPHB2, and EPHA4, since these are expressed by MZG (Mendes et al., 2006).

In summary we have demonstrated that rather than solely regulating axon guidance during telencephalic commissure formation, *Dcc* and *Ntn1* are critical genes required for IHF remodelling. Moreover, our study provides a novel role for axon guidance receptor DCC in regulating astroglial morphology, organisation and migration. Exemplified by *Ntn1* and *Dcc,* our study provides support for widespread consideration of astroglial development and IHF remodelling as possible underlying mechanisms regulated by these and other classically regarded “axon guidance genes” during CC formation.

Materials and Methods

EXPERIMENTAL MODELS AND SUBJECT DETAILS

Animals

Dcc$^{flox/flox}$ (Krimpenfort et al., 2012), *Dcc* knockout (Fazeli et al., 1997), *Dcc*^{kanga} (Finger et al., 2002), *Emx1*^{iCre} (Kessaris et al., 2006), *Ntn1-lacZ* (Serafini et al., 1996, and *tdTomato*$^{flox\_stop}$ (Madisen et al., 2010) mice on the C57BL/6J background and CD1 wildtype mice were bred at The University of Queensland. Prior approval for all breeding and experiments were obtained from the University of Queensland Animal Ethics Committee. Male and female mice were placed together overnight and the following morning was designated as E0 if a vaginal plug was detected. *Dcc* knockout and *Dcc*^{kanga} mice were genotyped by PCR and *Ntn1-lacZ* mice were tested for the presence of the *LacZ* gene and deemed homozygous if the β-galactosidase enzyme was trapped intracellularly, as previously described (Fazeli et al., 1997; Finger et al., 2002; Fothergill et al., 2014; Krimpenfort et al., 2012; Serafini et al., 1996). *Dcc*$^{flox/flox}$ mice were genotyped by the Australian Equine Genetics Research Centre at the University of Queensland.

Human subjects

Ethics for human experimentation was acquired by local ethics committees at The University of Queensland (Australia), the Royal Children's hospital (Australia), and UCSF Benioff Children's Hospital (USA). Genetic studies were performed previously (Marsh et al., 2017). Structural MR images were acquired as previously described (Marsh et al., 2017). In our study, we analysed the brain phenotype of affected individuals in family 2 (carrying *DCC* p.Val793Gly) and family 9 (carrying *DCC* p.Met1217Val;p.Ala1250Thr in cis) from our previous study.

METHOD DETAILS

Cell birth-dating and tissue collection

For cell birth dating studies, 5-ethynyl-2´-deoxyuridine (EdU; 5 mg per kg body weight, Invitrogen) dissolved in sterile phosphate buffer solution (PBS) was injected into the intraperitoneal cavity of awake pregnant dams. Brains were fixed via transcardial perfusion or immersion fixation with 4% paraformaldehyde (PFA).

Cell lines

HEK293 cells (from ATCC CRL-1573, not authenticated, free of mycoplasma contamination) were used to express alkaline phosphatase-conjugated NTN1

(NTN1-AP) in the supernatant of COS-7 cell culture. Although this cell line is commonly misidentified, this did not affect the conclusion of the binding assay done in COS-7 cells. U251 cells were obtained as U-373MG (RRID: CVCL_2219) but subsequently identified as U-251 via PCR-based short tandem repeat profiling. All cell lines were routinely tested for mycoplasma to ensure that cell lines were free of mycoplasma contamination. See the key resources table (supplementary file 2) for more information.

Cell culture

All cell lines were cultured at 37°C within a humidified atmosphere containing 5% CO_2 and immersed in Dulbecco's Modified Eagles Medium (DMEM) medium (Invitrogen or HyClone™), supplemented with 10% fetal bovine serum. U251 cells were plated on poly-d-lysine-coated coverslips (via submersion in 0.05 mg/mL solution, Sigma-Aldrich) at 10% confluence 24 hours prior to transfection. The pCAG-TDTOMATO, pCAG-H2B-GFP-2A-MyrTDTOMATO, pCAG-DCC:TDTOMATO and pCAG-DCC^{kanga}:TDTOMATO plasmids (1 µg) were transfected into the plated U251 cells using FuGENE 6 (Promega) in Opti-MEM (Gibco, Life Technologies). Cells were then grown for 20 hours and either fixed with 4% paraformaldehyde/4% sucrose or stimulated with ligand. Since 100ng/mL of recombinant NTN1 is sufficient to induce morphological changes in primary oligodendrocyte precursor cells (Rajasekharan et al., 2009), 200ng of recombinant mouse NTN1 protein (R&D Systems) was diluted in sterile PBS and added to cultures within 2 mL media. When ligand was added, cells were grown for a further 12 hours before fixation with 4% PFA/4% sucrose. N2A cells were cultured and transfected as outlined for the U251 cells except that after NTN1 stimulation, cells were cultured for only 8 hours before fixation. The pCAG-DCC:TDTOMATO wildtype and missense mutant receptor constructs (1.764 µg) were also transfected into HEK293T cells cultured on acid-washed coverslips using FuGENE HD (Promega) in Optimem (Gibco, Life Technologies). After 24 hours, cells were fixed with 4% PFA/4% sucrose.

NTN1-binding assay

Supernatant containing alkaline phosphatase-conjugated *NTN1* (*NTN1-AP*) was generated from expression in HEK293T cells as previously described (Zelina et

al., 2014). The pCAG-DCC:TDTOMATO wildtype and missense mutant receptor constructs (0.2 µg) were transfected into COS-7 cells using Lipofectamine® 2000 (Invitrogen). After 48 hours, cells were incubated with *NTN1*-AP supernatant (1:50) for 90 minutes at room temperature. Cells were washed and *NTN1*-binding activity was determined using colorimetric detection as previously described (Zelina et al., 2014).

Western blot

Whole-cell protein extracts were prepared from N2A and U251 cells, 20 hours after transfection with pCAG-DCC:TDTOMATO and pCAG-myr-TDTOMATO constructs (1µg) as previously described (Bunt et al., 2010). Moreover, COS-7 protein extracts were prepared 48 hours after transfection with the pCAG-DCC:TDTOMATO wildtype and missense mutant receptor constructs (0.2 µg). Western blots were performed to detect mouse DCC expression levels using a goat polyclonal anti-DCC antibody (1:200 COS-7 or 1:800, sc-6535, Santa Cruz Biotechnology), and mouse NTN1 using a goat polyclonal antibody (1:500 U251 or 1:1000 N2A, AF1109, R&D Systems) . GADPH was used as a loading control and was detected using rabbit monoclonal anti-GADPH antibodies (1:2000, 2118, Cell Signaling Technology for COS-7; 1:1000, IMG-5143A, IMGENEX for N2A and U251).

Immunohistochemistry

Brain sections were processed for standard fluorescence immunohistochemistry as previously described (Moldrich et al., 2010) with the following minor modifications: All sections were post-fixed on slides with 4% PFA and then subjected to antigen retrieval (125^{o}C for 4 minutes at 15 psi in sodium citrate buffer) prior to incubation with primary antibodies. Alexa Fluor IgG (Invitrogen), horseradish peroxidase-conjugated (Millipore) or biotinylated (Jackson Laboratories) secondary antibodies, used in conjunction with Alexa Fluor 647-conjugated Streptavidin (Invitrogen) amplification were used according to the manufacturer's instructions. EdU labeling was performed using the Click-iT EdU Alexa Fluor 488 Imaging Kit (Invitrogen). Cell nuclei were labeled using 4',6-diamidino-2-phenylindole, dihydrochloride (DAPI, Invitrogen) and coverslipped using ProLong Gold anti-fade reagent (Invitrogen) as mounting media. Primary antibodies used for immunohistochemistry were: rabbit anti-APC (1:250, ab15270, Abcam), mouse anti-α-dystroglycan (1:250, clone

IIH6C4, 05-593, Merk), rabbit anti-β-catenin (1:500, 9562, Cell signaling technology), mouse anti-β-dystroglycan (1:50, MANDAG2, 7D11, Developmental studies hybridoma bank), chicken anti β-galactosidase (1:500, ab9361, Abcam), rabbit anti-cleaved-caspase3 (1:500, 9661, cell signaling technology), goat anti-DCC (1:500, sc-6535, Santa cruz biotechnology), mouse anti-Gap43 (1:500; MAB347, Millipore), mouse anti-Gfap (1:500; MAB3402, Millipore), rabbit anti-Gfap (1:500; Z0334, Dako), mouse anti-Glast (or Eaat1; 1:500; ab49643, Abcam), rabbit anti-Glast (or Eaat1; 1:250; ab416, Abcam), mouse anti-Ki67 (1:500; 550609, BD Pharmingen), chicken anti-Laminin (1:500; LS-C96142, LSBio), rabbit anti-Laminin (1:500; L9393, Sigma), mouse anti-N-cadherin (CDH2; 1:250, 610921, BD Biosciences), rat anti-Nestin (NES; 1:50, AB 2235915, DSHB), chicken anti-Nestin (1:1000, ab134017, Abcam), goat anti-NTN1 (1:500; AF1109, R&D Systems), mouse anti-Neurofilament (1:500; MAB1621, Millipore), rabbit anti-Nfia (1:500; ARP32714, Aviva Systems Biology), rabbit anti-Nfib (1:500; HPA003956, Sigma), rabbit anti-neuronal-specific-ßIII-tubulin (1:500; ab18207, Abcam), rabbit anti-phospho p44/42 Mapk (or Erk1/2; 1:250; 9101, Cell Signaling Technology), rabbit anti-SOX9 (1:500, AB5535, Merck), and goat anti-TDTOMATO (1:500, ab8181-200, Sicgen). For actin staining, Alexa fluor-conjugated phalloidin (A22287, Thermofisher scientific) was incubated on tissue for thirty minutes in the dark as per the manufacturer's instructions, prior to the addition of primary antibodies. Immunohistochemistry was performed in a similar manner for cultured cells, with the following minor exceptions: HEK293T cells expressing wildtype and mutant pCAG-DCC:TDTOMATO constructs were not permeabilized to confirm exogenous DCC receptor localisation to the plasma membrane.

In situ hybridization

In situ hybridization was performed as previously described (Moldrich et al., 2010), with the following minor modifications: Fast red (Roche) was applied to detect probes with fluorescence. The *Fgf8* cDNA plasmid was a kind gift from Gail Martin, University of California, San Francisco. The *Ntn1* cDNA plasmid was provided by the Cooper lab. The *Mmp2* cDNA plasmid was generated by the Richards lab with the following primers: forward 5' - GAAGTATGGATTCTGTCCCGAG – 3' and reverse 5' – GCATCTACTTGCTGGACATCAG – 3'. The *Dcc* cDNA plasmid was generated by the Richards lab with the following primers, courtesy of the Allen Developing Brain

Atlas: forward 5’ - ATGGTGACCAAGAACAGAAGGT - 3’ and reverse 5’ – AATCACTGCTACAATCACCACG – 3’.

Plasmid expression constructs for cell culture and in utero electroporation

A TDTOMATO fluorophore (Clontech) was subcloned into a *pCAG* backbone to generate the pCAG-TDTOMATO plasmid. pCAG-H2B-GFP-2A-MyrTDTOMATO was provided by Arnold Kriegstein (University of California San Francisco). The *Dcc*-shRNA construct was provided by Xiong Zhiqi (Chinese Academy of Sciences, Shanghai; shRNA 1355 in Zhang et al., 2018). The *Dcc*-CRISPR nickase constructs were designed using the ATUM tool and obtained from ATUM to target *Dcc* exon 2 (*Dcc*-CRISPR 1, targeting chr18:71,954,969 - 71,955,009) and *Dcc* exon 3 (*Dcc*-CRISPR 2, targeting chr18:71,826,146 - 71,826,092). *Dcc*-CRISPR 1 had the maximum target score across the whole DCC coding sequence, while *Dcc*-CRISPR 1 had the maximum target score within exon 3 only.

To generate the pCAG-DCC:tdTomato plasmid, DCC:TDTOMATO (pmDCC:TDTOMATO; provided by Erik Dent, University of Wisconsin-Madison) was subcloned into the pCag-DsRed2 plasmid (Addgene, 15777, Cambridge, MA), by excising DsRed2.

For site-directed mutagenesis, the QuickChange II Site-Directed Mutagenesis Kit (Stratagene, Catalogue #200524) was used in accordance with the manufacturer’s instructions. The following primer pairs were used for site-directed mutagenesis:

p.Met743Leu: Forward 5’- GAGGAGGTGTCCAACTCAAGATGATACAGTTTGTCTG – 3’, reverse 5’ – CAGACAAACTGTATCATCTTGAGTTGGACACCTCCTC – 3’.

p.Val754Met: Forward 5’ – TAATATAGCCTCTCACCATGATGTTTGGGTTGAGAGG – 3’, reverse 5’ – CCTCTCAACCCAAACATCATGGTGAGAGGCTATATTA – 3’.

p.Ala893Thr: Forward 5’ – ACTTGTACTTGGTACTGGCAGAAAAGCTGGTCCT – 3’, reverse 5’ – AGGACCAGCTTTTCTGCCAGTACCAAGTACAAGT – 3’.

p.Val793Gl: Forward 5’ – ACTAGAGTCGAGTTCTCATTATGGAATCTCCTTAAAAGCTTTCAAC -3’, reverse 5’ – GTTGAAAGCTTTTAAGGAGATTCCATAATGAGAACTCGACTCTAGT – 3’.

p.Gly805Glu: Forward 5’ – CACTTTCGTAGAGAGGGACCTCTTCTCCGGCATTGTTGAA – 3’, reverse 5’ – TTCAACAATGCCGGAGAAGAGGTCCCTCTCTACGAAAGTG – 3’.

p.Met1217Val;p.Ala1250Thr: Forward 1 5' – GTTCCAAAGTGGACACGGAGCTGCCTGCGTC – 3', reverse 1 5' – GACGCAGGCAGCTCCGTGTCCACTTTGGAAC – 3', forward 2 5' – GTACAGGGATGGTACTCACAACAGCAGGATTACTGG – 3', reverse 2 5' - CCAGTAATCCTGCTGTTGTGAGTACCATCCCTGTAC – 3'.
p.Val848Arg: Forward 5' – CAGCCTGTACACCTCTTGGTGGGAGCATGGGGG – 3', reverse 5' – CCCCCATGCTCCCACCAAGAGGTGTACAGGCTG – 3'.
p.His857Ala: Forward 5' – ACCCTCACAGCCTCAGCGGTAAGAGCCACAGC – 3', reverse 5' – GCTGTGGCTCTTACCGCTGAGGCTGTGAGGG- 3'.
p.del-P3(Kanga): Forward 5' – CCACAGAGGATCCAGCCAGTGGAGATCCACC – 3', reverse 5' – GGTGGATCTCCACTGGCTGGATCCTCTGTGG – 3'.

In utero electroporation

In utero electroporation was performed as previously described (Suárez et al., 2014). Briefly, 2 µg/µL of *Dcc*-shRNA or *Dcc*-CRISPR were combined with 0.5 µg/µL TDTOMATO and 0.0025% Fast Green dye, and then microinjected into the lateral ventricles of E13 *Dcc*^{kanga} embryos. 5, 35 V square wave pulses separated by 100 ms were administered with 3mm paddles over the head of the embryo to direct the DNA into the cingulate cortex. Embryos were collected at E18 for analysis.

Image acquisition

Confocal images were acquired as either single 0.4-0.9 µm optical sections or multiple image projections of ~15-20 µm thick z-stacks using either an inverted Zeiss Axio-Observer fitted with a W1 Yokogawa spinning disk module, Hamamatsu Flash4.0 sCMOS camera and Slidebook 6 software, or an inverted Nikon TiE fitted with a Spectral Applied Research Diskovery spinning disk module, Hamamatsu Flash4.0 sCMOS camera and Nikon NIS software. Alternatively, for images of HEK293T cells, a LSM 780 confocal microscope was used. For imaging of NTN1-AP binding, a NanoZoomer 2.0-HT whole slide imager was used in conjunction with Hamamatsu (NDP_Viewer) software. For wide-field imaging of U251 and N2A cells stained for cleaved-caspase 3, Zen software (Carl Zeiss) was used to capture images on a Zeiss upright Axio-Imager fitted with Axio- Cam HRc camera. Images were pseudocolored to permit overlay, cropped, sized, and contrast-brightness enhanced for presentation with ImageJ and Adobe Photoshop software.

Measurements and cell quantification

Measurements of IHF length were performed using ImageJ v1.51s freeware (National Institutes of Health, Bethsda, USA). The length of the IHF within the interhemispheric midline was determined by comparing Laminin and DAPI-staining. To account for inter-brain variability, this length was then normalised to the entire length of the telencephalon along the interhemispheric midline, which was measured from the caudal-most point of the telencephalon to the rostral edge of cerebral hemispheres.

Cell proliferation and cell death in *Dcc*^{kanga} MZG was automatically counted using Imaris software (Bitplane) from a region of interest delineated by Glast staining, and excluding the IHF within a single z-slice. Cleaved-caspase 3-positive, TDTOMATO-positive N2A and U251 cells were manually counted using the cell counter plugin in ImageJ v1.51s freeware (National Institutes of Health, Bethsda, USA), from a 1187 x 954 µm region of interest.

The number of Sox9-positive cell bodies was counted manually using the Cell Counter plugin in ImageJ v1.51s freeware. Cell proliferation and cell death in tissue was automatically counted using Imaris software (Bitplane) from a region of interest delineated by Glast staining that excluded the IHF in a single z-slice.

The perimeter, circularity and area of U251 and N2A cells was measured from mean intensity projections of TDTOMATO images following thresholding in ImageJ v1.51s freeware (National Institutes of Health, Bethsda, USA). 48-191 cells per condition were analysed from 3-5 biological replicates.

Fluorescence intensity analysis

To compare fluorescence intensity, tissue sections were processed under identical conditions for immunofluorescence. Fluorescent images at 20x or 40x magnification were acquired using identical exposure settings for each fluorescent signal and identical number of slices through the z plane. A multiple intensity projection was created for each z-stack to create a 2D image. Identical regions of interest were outlined in ImageJ freeware and the fluorescence intensity was plotted versus the distance and the average fluorescence intensity was calculated.

Quantification and statistical analysis

A minimum of three animals were analysed for each separate phenotypic analysis. Sex was not determined for embryonic studies. A mix of male and female adult mice were used to determine the length of the IHF in *Dcc*^{kanga} and C57Bl/6 mice. All measurements and cell counting were performed on deidentified files so the researcher remained blind to the experimental conditions. For comparison between two groups, the data was first assessed for normality with a D'Agostino-Pearson omnibus normality test and then statistical differences between two groups were determined either with a parametric Student's t-test, or a non-parametric Mann-Whitney test in Prism software (v.6-v.8; GraphPad). To test whether CC or HC length was correlated with IHF length as normalised to total telencephalic midline length, the data was also assessed for normality with D'Agostino-Pearson omnibus normality tests, and a Pearson correlation coefficient was computed if the data was representative of a Gaussian distribution; otherwise, a nonparametric Spearman correlation was performed. For multiple comparisons of cell culture conditions or measurements of GFAP fluorescence across mouse strains, a Kruskal-Wallis test was performed with post-hoc Dunn's multiple comparison test. $p \leq 0.05$ was considered significantly different, where all p values are reported in text. All values are presented as mean ± standard error of the mean (SEM).

CONTACT FOR REAGENT AND RESOURCE SHARING

Further information and requests for resources and reagents should be directed to and will be fulfilled by Professor Linda J Richards (richards@uq.edu.au).

DATA AVAILABILITY

Microscopy data, measurements and statistical analyses are available. This study did not generate code.

Acknowledgements

We thank Marc Tessier-Lavigne for the *Ntn1-lacZ*, and *Dcc* knockout mouse lines, and Susan Ackermann (Jackson Laboratory) for the *Dcc*^{kanga} mouse lines. We thank colleagues for providing the constructs listed. We thank Luke Hammond, Rumelo Amor, Arnaud Guardin, Andrew Thompson and Matisse Jacobs for assistance with

microscopy, which was performed in the Queensland Brain Institute's Advanced Microscopy Facility. This work was supported by Australian NHMRC grants GNT456027, GNT631466, GNT1048849 and GNT1126153 to L.J.R and GNT1059666 to P.J.L and R.J.L, and USA National Institutes of Health grant 5R01NS058721 to E.S and L.J.R. R.S received an Australian Research Council DECRA fellowship (DE160101394). A.P.L.M and L.M were supported by a Research training program scholarship (Australian Postgraduate Award). A.P.L.M was further supported by an NHMRC Early Career Research Fellowship (APP1156820). AL.S.D was supported by an Australian Postgraduate award. L.M and AL.S.D received a Queensland Brain Institute Top-Up Scholarship. L.R.F was supported by a UQ Development Fellowship, R.J.L. was supported by a Melbourne Children's Clinician Scientist Fellowship and L.J.R. was supported by an NHMRC Principal Research Fellowship (GNT1120615).

We thank the families and members of the Australian Disorders of the Corpus Callosum (AusDoCC) for their support and time in being involved in this research. We thank the International Research Consortium for the Corpus Callosum and Cerebral Connectivity (IRC5, https://www.irc5.org) researchers for discussions and input.

Declaration of Interest

The authors declare no competing financial interests.

References

Abe, K., and Misawa, M. (2003). Astrocyte stellation induced by Rho kinase inhibitors in culture. Developmental Brain Research 143, 99-104.

Andrews, W., Liapi, A., Plachez, C., Camurri, L., Zhang, J., Mori, S., Murakami, F., Parnavelas, J.G., Sundaresan, V., and Richards, L.J. (2006). Robo1 regulates the development of major axon tracts and interneuron migration in the forebrain. Development 133, 2243-2252.

Antoine-Bertrand, J., Ghogha, A., Luangrath, V., Bedford, F.K., and Lamarche-Vane, N. (2011). The activation of ezrin-radixin-moesin proteins is regulated by netrin-1 through Src kinase and RhoA/Rho kinase activities and mediates netrin-1-induced axon outgrowth. Molecular Biology of the Cell 22, 3734-3746.

Arakawa, H. (2004). Netrin-1 and its receptors in tumorigenesis. Nature Reviews Cancer 4, 978-987.

Augusti-Tocco, G., and Sato, G. (1969). Establishment of functional clonal lines of neurons from mouse neuroblastoma. Proceedings of the National Academy of Sciences 64, 311-315.

Beggs, H.E., Schahin-Reed, D., Zang, K., Goebbels, S., Nave, K.-A., Gorski, J., Jones, K.R., Sretavan, D., and Reichardt, L.F. (2003). FAK deficiency in cells contributing to the basal lamina results in cortical abnormalities resembling congenital muscular dystrophies. Neuron 40, 501-514.

Brown, W.S., and Paul, L.K. (2019). The neuropsychological syndrome of agenesis of the corpus callosum. Journal of the International Neuropsychological Society, 1-7.

Bunt, J., de Haas, T. G., Hasselt, N. E., Zwijnenburg, D. A., Koster, J., Versteeg, R., & Kool, M. (2010). Regulation of cell cycle genes and induction of senescence by overexpression of OTX2 in medulloblastoma cell lines. Molecular Cancer Research 8, 1344-1357.

Chan, S.S., Zheng, H., Su, M.W., Wilk, R., Killeen, M.T., Hedgecock, E.M., and Culotti, J.G. (1996). UNC-40, a C. elegans homolog of DCC (Deleted in Colorectal Cancer), is required in motile cells responding to UNC-6 netrin cues. Cell 87.

Chen, Q., Sun, X., Zhou, X.-h., Liu, J.-h., Wu, J., Zhang, Y., and Wang, J.-h. (2013). N-terminal horseshoe conformation of DCC is functionally required for axon guidance and might be shared by other neural receptors. Journal of Cell Science 126, 186.

Conway, C.D., Howe, K.M., Nettleton, N.K., Price, D.J., Mason, J.O., and Pratt, T. (2011). Heparan sulfate sugar modifications mediate the functions of slits and other factors needed for mouse forebrain commissure development. Journal of Neuroscience 31, 1955-1970.

de la Torre, J.R., Höpker, V.H., Ming, G.-l., Poo, M.-m., Tessier-Lavigne, M., Hemmati-Brivanlou, A., and Holt, C.E. (1997). Turning of retinal growth cones in a Netrin-1 gradient mediated by the Netrin receptor DCC. Neuron 19, 1211-1224.

Derouiche, A., and Frotscher, M. (2001). Peripheral astrocyte processes: Monitoring by selective immunostaining for the actin- binding ERM proteins. Glia 36, 330-341.

Donahoo, A.-L.S., and Richards, L.J. (2009). Understanding the mechanisms of callosal development through the use of transgenic mouse models. In Seminars in Pediatric Neurology (Elsevier), pp. 127-142.

Edwards, T.J., Sherr, E.H., Barkovich, A.J., and Richards, L.J. (2014). Clinical, genetic and imaging findings identify new causes for corpus callosum development syndromes. Brain 137, 1579-1613.

Etienne-Manneville, S., and Hall, A. (2003). Cdc42 regulates GSK-3β and adenomatous polyposis coli to control cell polarity. Nature 421, 753-756.

Fazeli, A., Rayburn, H., Simons, J., Bronson, R.T., Gordon, J.I., Tessier-Lavigne, M., Weinberg, R.A., Dickinson, S.L., Hermiston, M.L., Tighe, R.V.*, et al.* (1997). Phenotype of mice lacking functional Deleted in colorectal cancer (Dcc) gene. Nature 386, 796-804.

Fenlon, L. R., and Richards, L. J. (2015). Contralateral targeting of the corpus callosum in normal and pathological brain function. Trends in Neurosciences, 38, 264-272.

Fenlon, L. R., Suárez, R., and Richards, L. J. (2017). The anatomy, organisation and development of contralateral callosal projections of the mouse somatosensory cortex. Brain and Neuroscience Advances, 1, 2398212817694888.

Finci, Lorenzo I., Krüger, N., Sun, X., Zhang, J., Chegkazi, M., Wu, Y., Schenk, G., Mertens, Haydyn D.T., Svergun, Dmitri I., Zhang, Y*., et al.* (2014). The crystal structure of Netrin-1 in complex with DCC reveals the bifunctionality of Netrin-1 as a guidance cue. Neuron 83, 839-849.

Finger, J.H., Bronson, R.T., Harris, B., Johnson, K., Przyborski, S.A., and Ackerman, S.L. (2002). The Netrin 1 receptors Unc5h3 and Dcc are necessary at multiple choice points for the guidance of corticospinal tract axons. The Journal of Neuroscience 22, 10346-10356.

Fothergill, T., Donahoo, A.L., Douglass, A., Zalucki, O., Yuan, J., Shu, T., Goodhill, G.J., and Richards, L.J. (2014). Netrin-DCC signaling regulates corpus callosum formation through attraction of pioneering axons and by modulating Slit2-mediated repulsion. Cerebral Cortex.

Gad, J.M., Keeling, S.L., Shu, T., Richards, L.J., and Cooper, H.M. (2000). The spatial and temporal expression patterns of Netrin receptors, DCC and Neogenin, in the developing mouse retina. Experimental Eye Research 70, 711-722.

Glass, H.C., Shaw, G.M., Ma, C., and Sherr, E.H. (2008). Agenesis of the corpus callosum in California 1983–2003: A population- based study. American Journal of Medical Genetics Part A 146, 2495-2500.

Gobius, I., Morcom, L., Suárez, R., Bunt, J., Bukshpun, P., Reardon, W., Dobyns, William B., Rubenstein, John L.R., Barkovich, A.J., Sherr, Elliott H., and Richards, Linda J. (2016). Astroglial-mediated remodeling of the interhemispheric midline is required for the formation of the corpus callosum. Cell Reports 17, 735-747.

Gobius, I., and Richards, L.J. (2011). Creating connections in the developing brain: mechanisms regulating corpus callosum development, Vol 2. (San Rafael, Calif: Morgan & Claypool Publishers).

Goto, J., Tezuka, T., Nakazawa, T., Sagara, H., and Yamamoto, T. (2008). Loss of Fyn tyrosine kinase on the C57BL/6 genetic background causes hydrocephalus with defects in oligodendrocyte development. Molecular and Cellular Neuroscience 38, 203-212.

Hagedorn, E.J., Ziel, J.W., Morrissey, M.A., Linden, L.M., Wang, Z., Chi, Q., Johnson, S.A., and Sherwood, D.R. (2013). The netrin receptor DCC focuses invadopodia-driven basement membrane transmigration in vivo. The Journal of Cell Biology 201, 903-913.

Hakanen, J., and Salminen, M. (2015). Defects in neural guidepost structures and failure to remove leptomeningeal cells from the septal midline behind the interhemispheric fusion defects in Netrin1 deficient mice. International Journal of Developmental Neuroscience 47, 206-215.

Hedgecock, E.M., Culotti, J.G., and Hall, D.H. (1990). The unc-5, unc-6, and unc-40 genes guide circumferential migrations of pioneer axons and mesodermal cells on the epidermis in C. elegans. Neuron 4.

Jamuar, S.S., Schmitz-Abe, K., D'Gama, A.M., Drottar, M., Chan, W.-M., Peeva, M., Servattalab, S., Lam, A.-T.N., Delgado, M.R., and Clegg, N.J. (2017). Biallelic mutations in human DCC cause developmental split-brain syndrome. Nature Genetics 49, 606.

Jarjour, A.A., Durko, M., Luk, T.L., Marçal, N., Shekarabi, M., and Kennedy, T.E. (2011). Autocrine Netrin function inhibits glioma cell motility and promotes focal adhesion formation. PloS one 6, e25408.

Keino-Masu, K., Masu, M., Hinck, L., Leonardo, E.D., Chan, S.S.Y., Culotti, J.G., and Tessier-Lavigne, M. (1996). Deleted in colorectal cancer (DCC) encodes a netrin receptor. Cell 87, 175-185.

Kennedy, T.E., Serafini, T., de la Torre, J.R., and Tessier-Lavigne, M. (1994). Netrins are diffusible chemotropic factors for commissural axons in the embryonic spinal cord. Cell 78.

Kessaris, N., Fogarty, M., Iannarelli, P., Grist, M., Wegner, M., and Richardson, W.D.

(2006). Competing waves of oligodendrocytes in the forebrain and postnatal

elimination of an embryonic lineage. Nature Neuroscience 9, 173.

Kolodziej, P.A., Timpe, L.C., Mitchell, K.J., Fried, S.R., Goodman, C.S., Jan, L.Y., and Jan, Y.N. (1996). Frazzled encodes a Drosophila member of the DCC immunoglobulin subfamily and is required for CNS and motor axon guidance. Cell 87.

Krimpenfort, P., Song, J.-Y., Proost, N., and Zevenhoven, J. (2012). Deleted in colorectal carcinoma suppresses metastasis in p53-deficient mammary tumours. Nature 482, 538.

Lavialle, M., Aumann, G., Anlauf, E., Pröls, F., Arpin, M., and Derouiche, A. (2011). Structural plasticity of perisynaptic astrocyte processes involves ezrin and metabotropic glutamate receptors. Proceedings of the National Academy of Sciences of the United States of America 108, 12915-12919.

Li, W., Lee, J., Vikis, H.G., Lee, S.-H., Liu, G., Aurandt, J., Shen, T.-L., Fearon, E.R., Guan, J.-L., and Han, M. (2004). Activation of FAK and Src are receptor-proximal events required for netrin signaling. Nature Neuroscience 7, 1213-1221.

Llambi, F., Causeret, F., Bloch-Gallego, E., and Mehlen, P. (2001). Netrin-1 acts as a survival factor via its receptors UNC5H and DCC. The EMBO journal 20, 2715-2722.

Madisen, L., Zwingman, T.A., Sunkin, S.M., Oh, S.W., Zariwala, H.A., Gu, H., Ng, L.L., Palmiter, R.D., Hawrylycz, M.J., Jones, A.R. and Lein, E.S., 2010. A robust and high-throughput Cre reporting and characterization system for the whole mouse brain. Nature Neuroscience, 13, 133 –140.

Marsh, A.P., Edwards, T.J., Galea, C., Cooper, H.M., Engle, E.C., Jamuar, S.S., Méneret, A., Moutard, M.L., Nava, C., and Rastetter, A. (2018). DCC mutation update: Congenital mirror movements, isolated agenesis of the corpus callosum, and developmental split brain syndrome. Human Mutation 39, 23-39.

Marsh, A.P.L., Heron, D., Edwards, T.J., Quartier, A., Galea, C., Nava, C., Rastetter, A., Moutard, M.-L., Anderson, V., Bitoun, P*., et al.* (2017). Mutations in DCC cause isolated agenesis of the corpus callosum with incomplete penetrance. Nature Genetics 49, 511-514.

1117 Mehlen, P., Rabizadeh, S., Snipas, S.J., Assa-Munt, N., and Salvesen, G.S.
1118 (1998). The DCC gene product induces apoptosis by a mechanism requiring
1119 receptor proteolysis. Nature 395, 801-804.

1120 Mendes, S.W., Henkemeyer, M., and Liebl, D.J. (2006). Multiple Eph receptors and
1121 B-class ephrins regulate midline crossing of corpus callosum fibers in the
1122 developing mouse forebrain. The Journal of Neuroscience 26, 882-892.

1123 Menzies, A.S., Aszodi, A., Williams, S.E., Pfeifer, A., Wehman, A.M., Goh, K.L.,
1124 Mason, C.A., Fassler, R., and Gertler, F.B. (2004). Mena and Vasodilator-
1125 stimulated phosphoprotein are required for multiple actin-dependent processes
1126 that shape the vertebrate nervous system. The Journal of Neuroscience 24,
1127 8029.

1128 Moldrich, R.X., Gobius, I., Pollak, T., Zhang, J., Ren, T., Brown, L., Mori, S., De
1129 Juan Romero, C., Britanova, O., Tarabykin, V., and Richards, L.J. (2010).
1130 Molecular regulation of the developing commissural plate. J Comp Neurol 518,
1131 3645-3661.

1132 Morcom, L.R., Edwards, T.J., and Richards, L.J. (2016). Chapter 14 - Cortical
1133 architecture, midline guidance, and tractography of 3D white matter tracts. In
1134 Axons and Brain Architecture, K.S. Rockland, ed. (San Diego: Academic
1135 Press), pp. 289-313.

1136 Morcom, L., Edwards, T.J., Rider, E., Jones-Davis, D., Lim, J.W., Chen, K.S.,
1137 Dean, R., Bunt, J., Ye, Y., Gobius, I. and Suárez, R., Mandelstam, S., Sherr,
1138 E.H., and Richards, L.J. (2020). DRAXIN regulates interhemispheric fissure
1139 remodelling to influence the extent of corpus callosum formation. *bioRxiv*.

1140 Müller, H., and Soares, M.J. (2006). Alkaline phosphatase fusion proteins as tags
1141 for identifying targets for placental ligands. In Placenta and Trophoblast
1142 (Springer), pp. 331-340.

1143 Murk, K., Blanco Suarez, E.M., Cockbill, L.M.R., Banks, P., and Hanley, J.G.
1144 (2013). The antagonistic modulation of Arp2/3 activity by N-WASP, WAVE2
1145 and PICK1 defines dynamic changes in astrocyte morphology. Journal of Cell
1146 Science 126, 3873-3883.

Paul, L.K., Brown, W.S., Adolphs, R., Tyszka, J.M., Richards, L.J., Mukherjee, P., and Sherr, E.H. (2007). Agenesis of the corpus callosum: genetic, developmental and functional aspects of connectivity. Nat Rev Neurosci 8, 287-299.

Probst, M. (1901). The structure of complete dissolving corpus callosum of the cerebrum and also the microgyry and heterotropy of the grey substance. Archiv Fur Psychiatrie und Nervenkrankheiten 34, 709-786.

Qu, C., Dwyer, T., Shao, Q., Yang, T., Huang, H., and Liu, G. (2013). Direct binding of TUBB3 with DCC couples netrin-1 signaling to intracellular microtubule dynamics in axon outgrowth and guidance. Journal of Cell Science 126, 3070-3081.

Racchetti, G., D'Alessandro, R., and Meldolesi, J. (2012). Astrocyte stellation, a process dependent on Rac1 is sustained by the regulated exocytosis of enlargeosomes. Glia 60, 465-475.

Rajasekharan, S., Baker, K.A., Horn, K.E., Jarjour, A.A., Antel, J.P., and Kennedy, T.E. (2009). Netrin 1 and Dcc regulate oligodendrocyte process branching and membrane extension via Fyn and RhoA. Development 136, 415-426.

Rakic, P., and Yakovlev, P.I. (1968). Development of the corpus callosum and cavum septi in man. The Journal of Comparative Neurology 132, 45-72.

Ren, T., Zhang, J., Plachez, C., Mori, S., and Richards, L.J. (2007). Diffusion tensor magnetic resonance imaging and tract-tracing analysis of Probst bundle structure in Netrin1-and DCC-deficient mice. The Journal of Neuroscience 27, 10345-10349.

Serafini, T., Colamarino, S.A., Leonardo, E.D., Wang, H., Beddington, R., Skarnes, W.C., and Tessier-Lavigne, M. (1996). Netrin-1 is required for commissural axon guidance in the developing vertebrate nervous system. Cell 87.

Shea, T.B., Fischer, I., and Sapirstein, V.S. (1985). Effect of retinoic acid on growth and morphological differentiation of mouse NB2a neuroblastoma cells in culture. Developmental Brain Research 21, 307-314.

1176 Shekarabi, M., and Kennedy, T.E. (2002). The netrin-1 receptor DCC promotes
1177 filopodia formation and cell spreading by activating Cdc42 and Rac1. Molecular
1178 and Cellular Neuroscience 19, 1-17.

1179 Shekarabi, M., Moore, S.W., Tritsch, N.X., Morris, S.J., Bouchard, J.-F., and
1180 Kennedy, T.E. (2005). Deleted in Colorectal Cancer binding Netrin-1 mediates
1181 cell substrate adhesion and recruits Cdc42, Rac1, Pak1, and N-WASP into an
1182 intracellular signaling complex that promotes growth cone expansion. Journal
1183 of Neuroscience 25, 3132-3141.

1184 Shen, Y., Mani, S., and Meiri, K.F. (2004). Failure to express GAP-43 leads to
1185 disruption of a multipotent precursor and inhibits astrocyte differentiation.
1186 Molecular and Cellular Neuroscience 26, 390-405.

1187 Shu, T., Valentino, K.M., Seaman, C., Cooper, H.M., and Richards, L.J. (2000).
1188 Expression of the netrin-1 receptor, deleted in colorectal cancer (DCC), is
1189 largely confined to projecting neurons in the developing forebrain. The Journal
1190 of Comparative Neurology 416, 201-212.

1191 Silver, J., Edwards, M.A., and Levitt, P. (1993). Immunocytochemical
1192 demonstration of early appearing astroglial structures that form boundaries and
1193 pathways along axon tracts in the fetal brain. The Journal of Comparative
1194 Neurology, 328, 415-436.

1195 Silver, J., Lorenz, S.E., Wahlsten, D., and Coughlin, J. (1982). Axonal guidance
1196 during development of the great cerebral commissures: descriptive and
1197 experimental studies, in vivo, on the role of preformed glial pathways. The
1198 Journal of Comparative Neurology 210, 10-29.

1199 Stein, E., and Tessier-Lavigne, M. (2001). Hierarchical organization of guidance
1200 receptors: silencing of netrin attraction by slit through a Robo/DCC receptor
1201 complex. Science 291, 1928-1938.

1202 Suarez, R. (2017). Evolution of telencephalic commissures: Conservation and
1203 change of developmental systems in the origin of brain wiring novelties. In:
1204 Evolution of Nervous Systems (Second Edition) (Kaas JH, ed), pp 205-223.
1205 Oxford: Academic Press.

Suárez, R., Fenlon, L. R., Marek, R., Avitan, L., Sah, P., Goodhill, G. J., and Richards, L. J. (2014). Balanced interhemispheric cortical activity is required for correct targeting of the corpus callosum. Neuron 82, 1289-1298.

Suárez, R., Gobius, I., and Richards, L. J. (2014). Evolution and development of interhemispheric connections in the vertebrate forebrain. Frontiers in Human Neuroscience, 8, 497.

Suárez, R., Paolino, A., Fenlon, L. R., Morcom, L. R., Kozulin, P., Kurniawan, N. D., & Richards, L. J. (2018). A pan-mammalian map of interhemispheric brain connections predates the evolution of the corpus callosum. Proceedings of the National Academy of Sciences, 115, 9622-9627.

Sun, K.L.W., Correia, J.P., and Kennedy, T.E. (2011). Netrins: versatile extracellular cues with diverse functions. Development 138, 2153-2169.

Sun, W., Cornwell, A., Li, J., Peng, S., Osorio, M.J., Aalling, N., Wang, S., Benraiss, A., Lou, N., and Goldman, S.A. (2017). SOX9 is an astrocyte-specific nuclear marker in the adult brain outside the neurogenic regions. Journal of Neuroscience 37, 4493-4507.

Tischfield, M.A., Baris, H.N., Wu, C., Rudolph, G., Van Maldergem, L., He, W., Chan, W.-M., Andrews, C., Demer, J.L., Robertson, R.L.*, et al.* (2010). Human TUBB3 mutations perturb microtubule dynamics, kinesin interactions, and axon guidance. Cell 140, 74-87.

Tomasch, J. (1954). Size, distribution, and number of fibres in the human corpus callosum. Anat Rec 119, 119-135.

Unni, D.K., Piper, M., Moldrich, R.X., Gobius, I., Liu, S., Fothergill, T., Donahoo, A.-L.S., Baisden, J.M., Cooper, H.M., and Richards, L.J. (2012). Multiple Slits regulate the development of midline glial populations and the corpus callosum. Developmental Biology 365, 36-49.

Varadarajan, S.G., Kong, J.H., Phan, K.D., Kao, T.-J., Panaitof, S.C., Cardin, J., Eltzschig, H., Kania, A., Novitch, B.G., and Butler, S.J. (2017). Netrin1 produced by neural progenitors, not floor plate cells, is required for axon guidance in the spinal cord. Neuron 94, 790-799.

Wei, Z., Yan, J., Lu, Q., Pan, L., and Zhang, M. (2011). Cargo recognition mechanism of myosin X revealed by the structure of its tail MyTH4-FERM tandem in complex with the DCC P3 domain. Proceedings of the National Academy of Sciences 108, 3572.

Xu, S., Liu, Y., Li, X., Liu, Y., Meijers, R., Zhang, Y., and Wang, J.-h. (2018). The binding of DCC-P3 motif and FAK-FAT domain mediates the initial step of netrin-1/DCC signaling for axon attraction. Cell Discovery 4, 8.

Yokota, Y., Eom, T.-Y., Stanco, A., Kim, W.-Y., Rao, S., Snider, W.D., and Anton, E.S. (2010). Cdc42 and Gsk3 modulate the dynamics of radial glial growth, inter-radial glial interactions and polarity in the developing cerebral cortex. Development 137, 4101-4110.

Yokota, Y., Kim, W.-Y., Chen, Y., Wang, X., Stanco, A., Komuro, Y., Snider, W., and Anton, E.S. (2009). The Adenomatous Polyposis Coli Protein is an essential regulator of radial glial polarity and construction of the cerebral cortex. Neuron 61, 42-56.

Yoo, S.-W., Motari, M.G., and Schnaar, R.L. (2017). Agenesis of the corpus callosum in Nogo receptor deficient mice. Journal of Comparative Neurology 525, 291-301.

Yung, A. R., Nishitani, A. M., and Goodrich, L. V. (2015). Phenotypic analysis of mice completely lacking netrin 1. Development, 142, 3686-3691.

Zelina, P., Blockus, H., Zagar, Y., Péres, A., Friocourt, F., Wu, Z., Rama, N., Fouquet, C., Hohenester, E., and Tessier-Lavigne, M. (2014). Signaling switch of the axon guidance receptor Robo3 during vertebrate evolution. Neuron 84, 1258-1272.

Zeug, A., Müller, F.E., Anders, S., Herde, M.K., Minge, D., Ponimaskin, E., and Henneberger, C. (2018). Control of astrocyte morphology by Rho GTPases. Brain Research Bulletin 136, 44-53.

Zhang, J.H., Zhao, Y.F., He, X.X., Zhao, Y., He, Z.X., Zhang, L., Huang, Y., Wang, Y.B., Hu, L., Liu, L. and Yu, H.L. (2018). DCC-mediated Dab1 phosphorylation participates in the multipolar-to-bipolar transition of migrating neurons. Cell Reports 22, 3598-3611.

Zhang, S., Xie, R., Wan, F., Ye, F., Guo, D., and Lei, T. (2013). Identification of U251 glioma stem cells and their heterogeneous stem- like phenotypes. Oncology Letters 6, 1649-1655.

Ziel, J.W., Hagedorn, E.J., Audhya, A., and Sherwood, D.R. (2009). UNC-6 (netrin) orients the invasive membrane of the anchor cell in C. elegans. Nature Cell Biology 11, 183.

Figures and legends

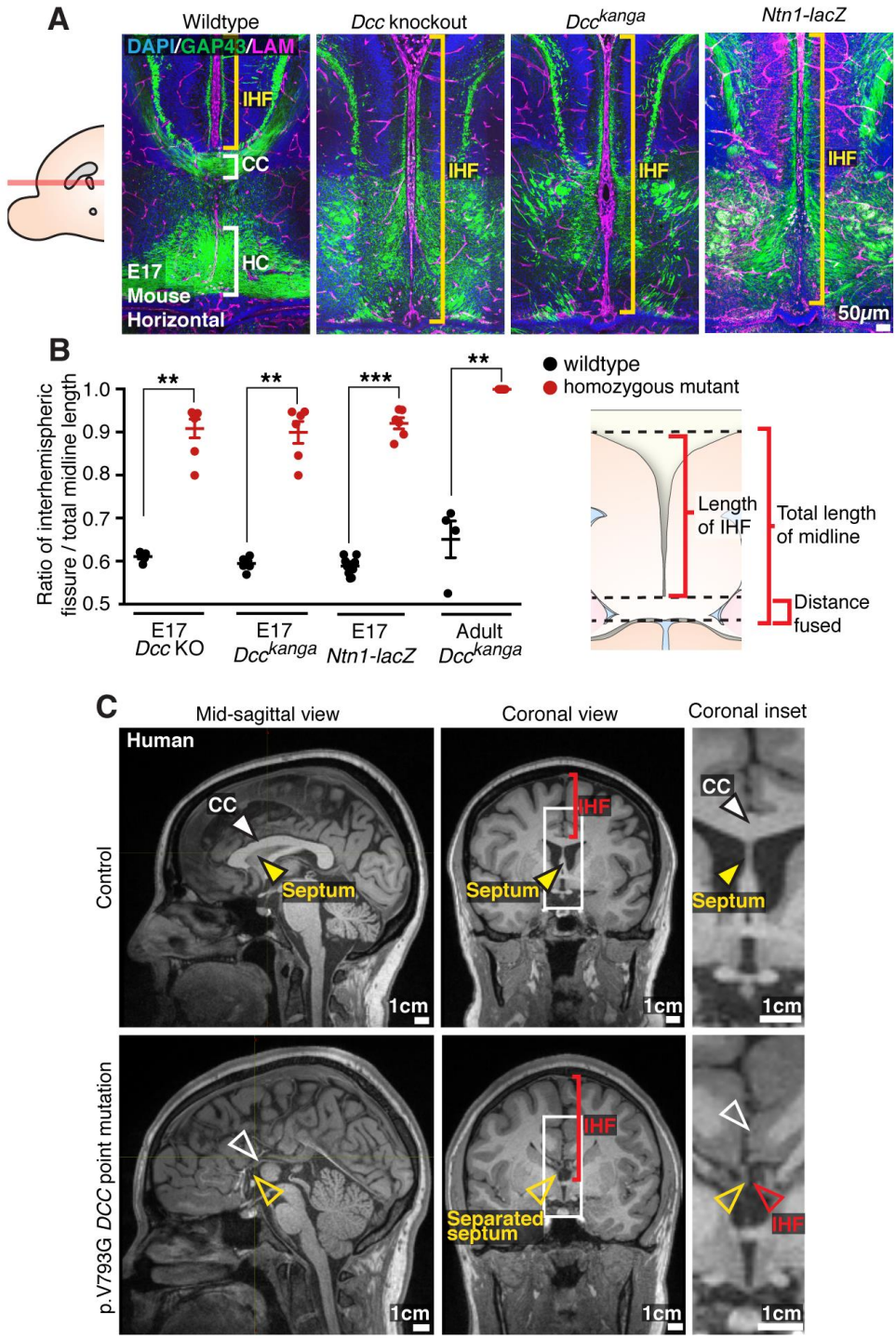

Figure 1: NTN1 and DCC are crucial for remodelling of the IHF, CC and HC formation

(A) Staining for Gap43-positive axons (green) and pan-Laminin (LAM)-positive leptomeninges and basement membrane (magenta) in wildtype, *Dcc* knockout, Dcc^{kanga}, and *Ntn1-lacZ* mice at E17, indicate midline formation or absence of the CC and HC (white brackets) and extent of the IHF (yellow brackets).

(B) The ratio of IHF length over the total midline length with schema.

(C) T1-weighted MR images of a control subject compared with an individual with a DCC mutation demonstrate the presence or absence of the CC (white arrowheads) and extent of the IHF (red arrowheads and brackets) within the septum (yellow arrowheads).

Graph represents mean ± SEM. Statistics by Mann-Whitney test: **p < 0.01, ***p < 0.001. See related Figure 1-figure supplement 1 and Supplementary File 1.

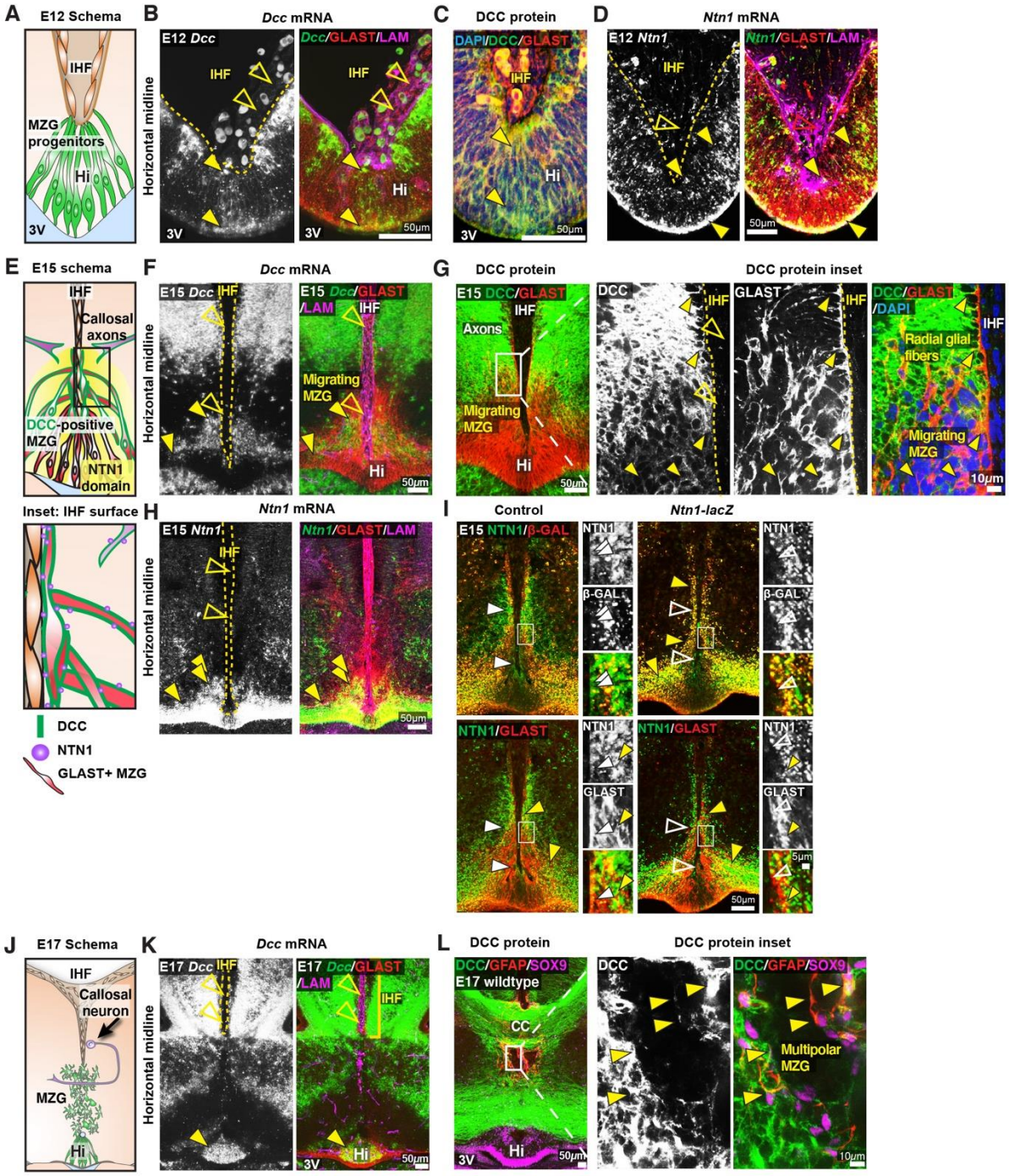

Figure 2: DCC and NTN1 are expressed in MZG and MZG progenitors

(A, E, and J) Schematics depicting the cellular composition of the ventral telencephalic midline at E12, E15 and E17.

(B, F and K) *Dcc* mRNA (green), Glast-positive glia (red), and pan-laminin (LAM)-positive leptomeninges and basement membrane (magenta) in E12, E15, and E17 wildtype mice reveal *Dcc*-positive/Glast-positive glial fibers (yellow arrowheads) and absence of *Dcc* within the IHF (open yellow arrowheads).

(C and G) DCC protein (green) and Glast protein (red) at E12 and E15 in wildtype mice reveal DCC-positive/Glast-positive glial fibers (yellow arrowheads) and absence of DCC within the IHF (open yellow arrowheads).

(D and H) *Ntn1* mRNA (green), Glast (red) and pan-LAM (magenta) in E12 and E15 wildtype mice show *Ntn1*-positive/Glast-positive glial fibers (yellow arrowheads) and absence of *Ntn1* within the IHF (open yellow arrowheads).

(E inset) Schema of DCC and NTN1 expression at the E15 IHF surface, based on the results from F-I and Figure 2-figure supplement 1.

(I) NTN1 (green) and Glast (red) or β-galactosidase (β-GAL; red) immunolabelling in E15 control and *Ntn1-lacZ* mice identify regions of NTN1 staining present in control heterozygotes and absent in homozygous *Ntn1-lacZ* mice (white arrowheads) and NTN1-/β-GAL-positive puncta located in Glast-positive glia (yellow arrowheads), with insets.

(L) DCC protein (green), glial-specific nuclear marker SOX9 (magenta) and mature astroglial marker (GFAP) in E17 wildtype mice identify DCC-positive/GFAP-positive/SOX9-positive glia (yellow arrowheads). 3V = third ventricle, Hi = telencephalic hinge, See related Figure 2-figure supplement 1.

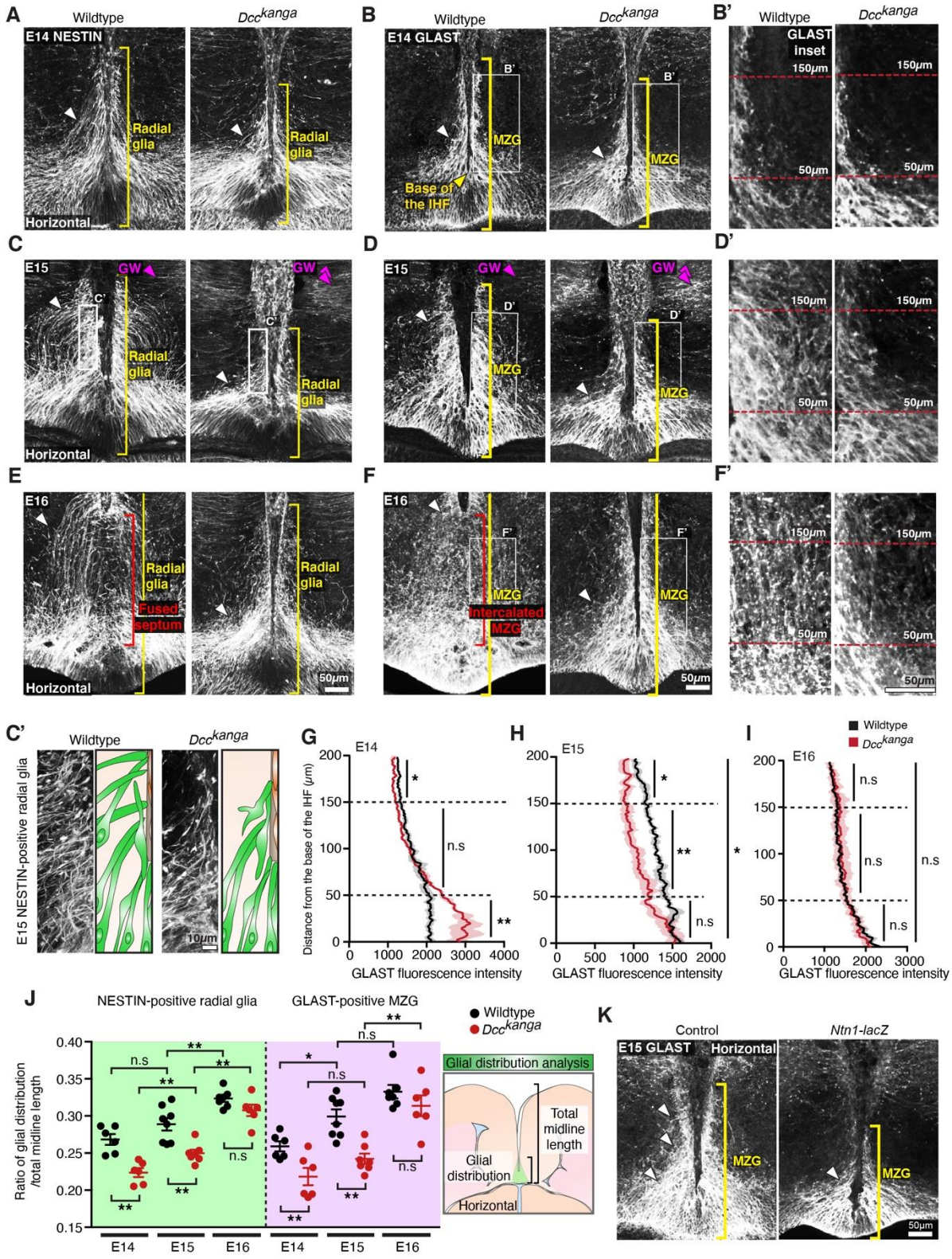

Figure 3: NTN1 and DCC regulate MZG morphology and spatial distribution

Nestin-positive radial glia (white; A, C and E) and Glast-positive glia (white; B, D, F and K) in E14 - E16 *Dcc*^{kanga} mice (A-F) and E15 *Ntn1-LacZ* mice (K) demonstrate the distribution of glial processes along the IHF surface (yellow brackets) and lateral

to the lHF (white arrowheads) with insets (C', B', D' and F'). Radial fibers of the glial wedge (GW) are indicated with magenta arrowheads.

The mean fluorescence intensity of Glast staining between wildtype and *Dcc*^{kanga} mice at E14 (G), E15 (H) and E16 (I) based on the results from B, D and F, respectively.

(J) The ratio of glial distribution over total midline length, with schema, based on the results from A-F.

All graphs represent mean ± SEM. Statistics by Mann-Whitney test (C), or a Two-way ANOVA test with post Sidak's multiple comparison test (D): n.s = not significant, *p < 0.05, **p < 0.01. See related Figure 3-figure supplement 1 and Supplementary File 1.

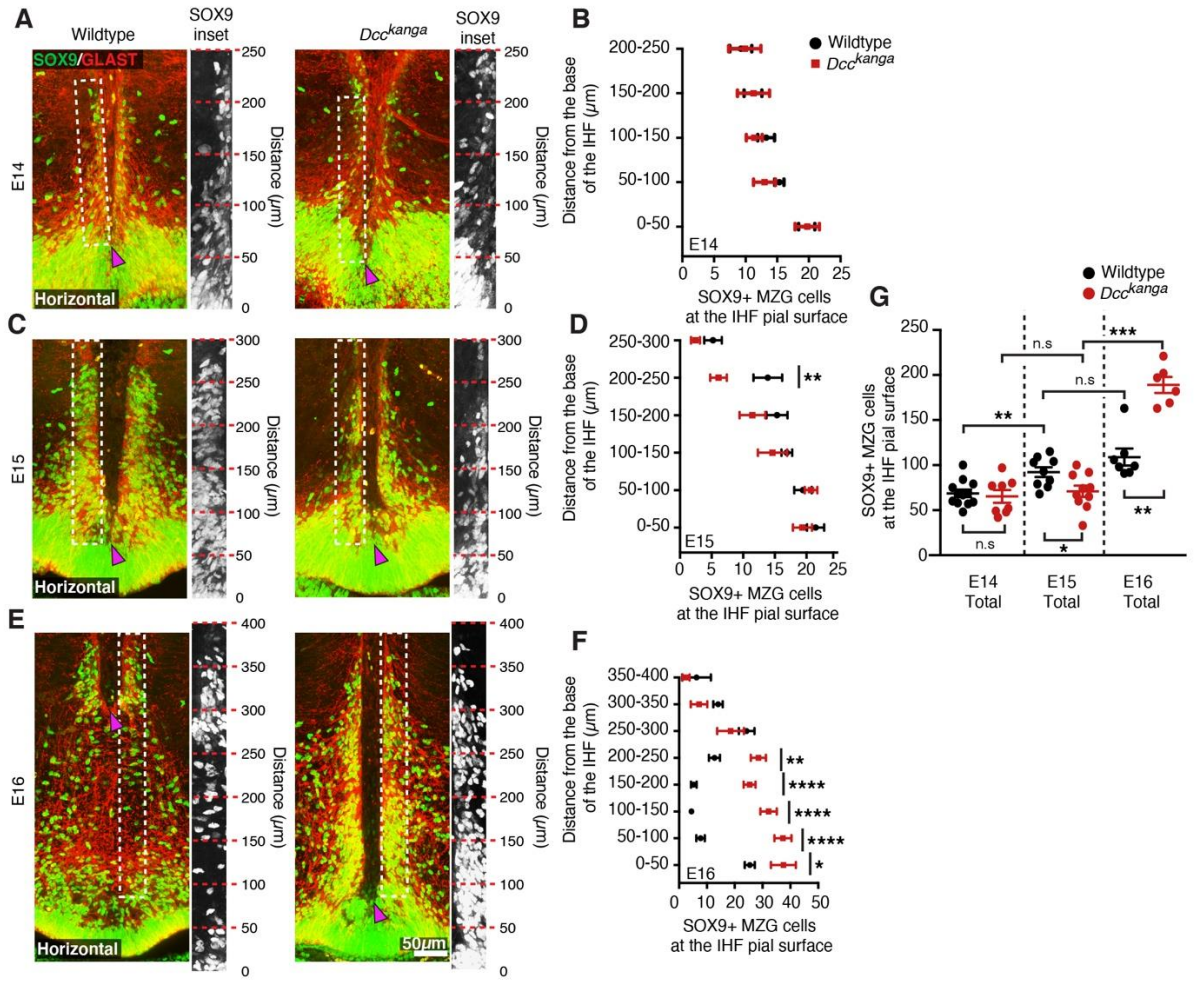

Figure 4: DCC regulates MZG migration to the IHF surface

(A, C, E) Nuclear glial marker SOX9 (green) and MZG marker Glast (red), in E14-E16 *Dcc*^{kanga} mice reveal SOX9-positive/Glast-positive MZG at the pial IHF surface (boxed region and insets) above the base of the IHF (magenta arrowhead).

(B, D, F, G) Quantification of SOX9-positive/Glast-positive MZG at the IHF pial surface based on the results from A, C and E.

All graphs represent mean ± SEM. Statistics by Mann-Whitney test (E) or Two-way ANOVA with post Sidak's multiple comparison test (B-D): *p < 0.05, **p < 0.01, ***p < 0.001, ****p < 0.0001, n.s = not significant. See related Figure 4-figure supplement 1 and Supplementary File 1.

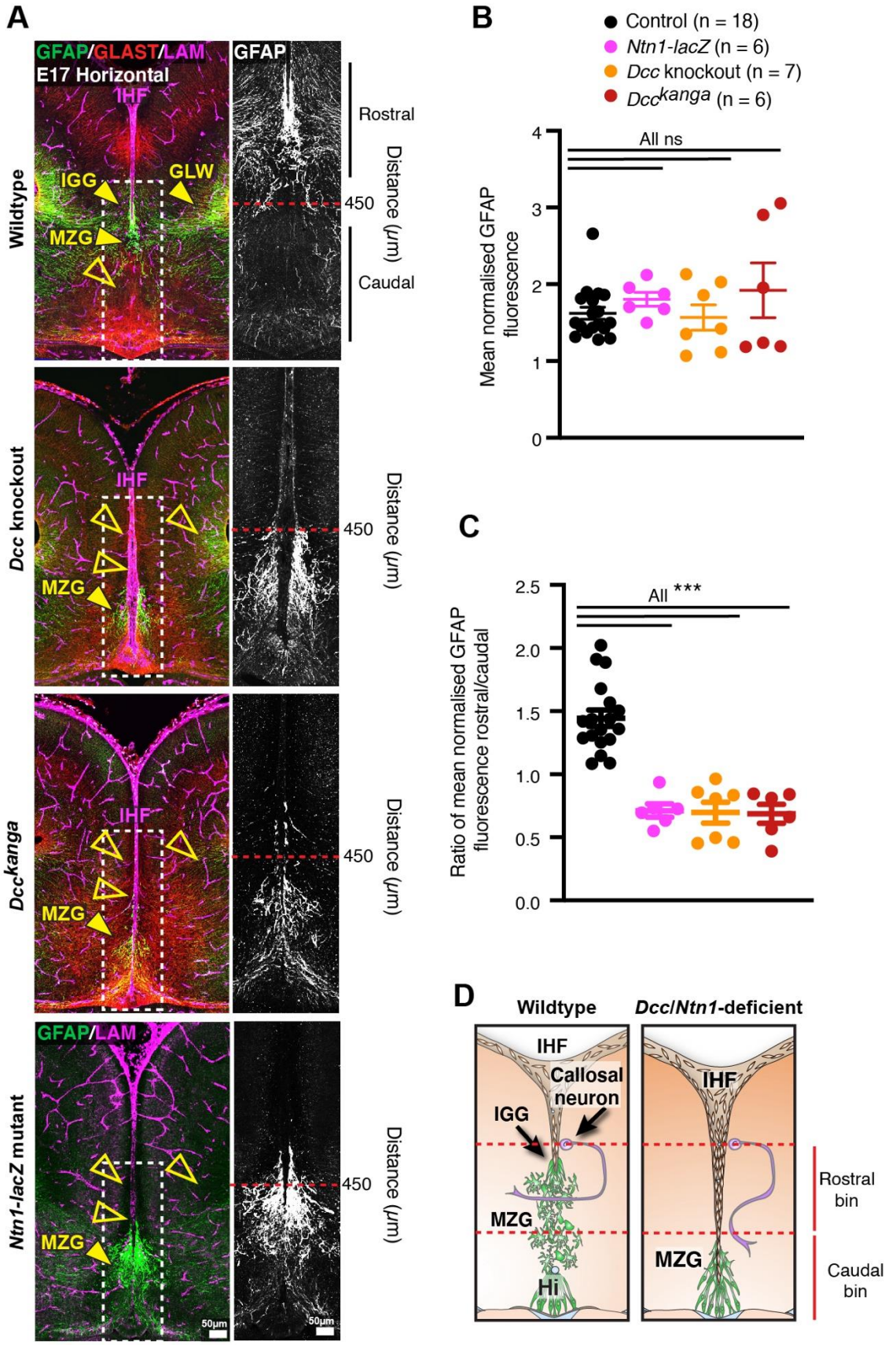

Figure 5: NTN1 and DCC regulate MZG organisation during IHF remodelling

(A) Gfap-positive mature astroglia (green or white in inset), Glast-positive glia (red), and pan-Laminin (LAM)-positive IHF and basement membrane (magenta) in E17 wildtype *Dcc*^{kanga}, *Dcc* knockout, and *Ntn1-LacZ* mice. Yellow arrowheads indicate presence (filled) or absence (open) of midline glial populations, the midline zipper glia (MZG), indusium griseum glia (IGG) and glial wedge (GW). Fluorescence intensity of Gfap staining from insets or bins in insets (red dotted line) was quantified in B and C.

(D) Schema of MZG development, IHF remodelling and CC formation in wildtype mice and mice deficient for NTN1 or DCC. Red dotted lines indicate rostral and caudal bins that were used to calculate the ratio of GFAP fluorescence in C.

All graphs represent mean ± SEM. Statistics by Kruskal-Wallis test with post-hoc Dunn's multiple comparison test. ***p < 0.001, n.s = not significant. See related Figure 4-figure supplement 1, Figure 5-figure supplemnent 5 and Supplementary File 1.

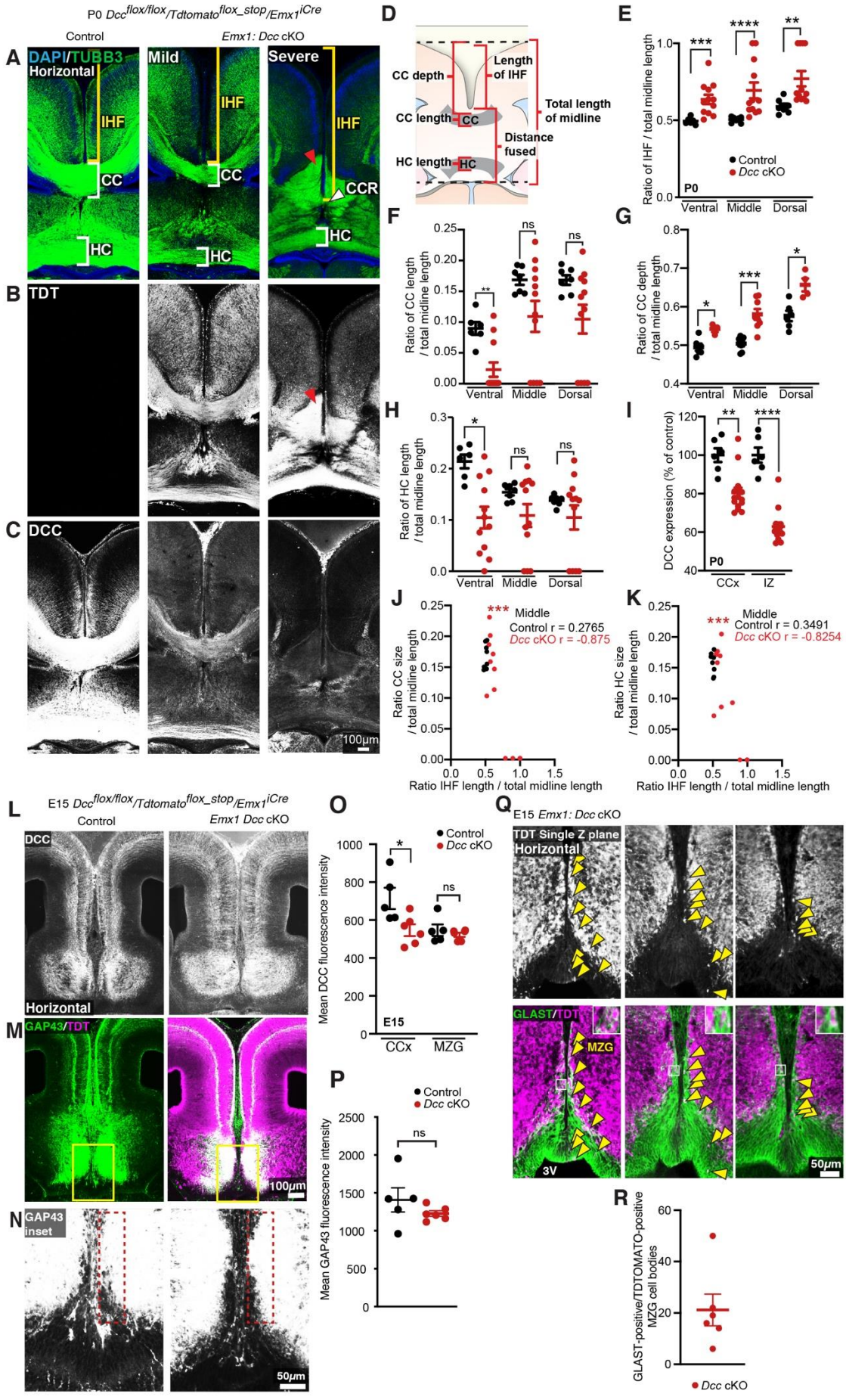
P0 Dcc flox/flox /Tdtomato flox_stop /Emx1 iCre
Control
Emx1: Dcc cKO
A
DAPI/TUBB3
Horizontal
Mild
Severe
IHF
CC
HC
CCR
B
TDT
C
DCC
100μm
D
CC depth
Length of IHF
CC length
Total length of midline
Distance fused
HC length
E
Ratio of IHF / total midline length
Control
Dcc cKO
P0
Ventral
Middle
Dorsal
F
Ratio of CC length / total midline length
G
Ratio of CC depth / total midline length
H
Ratio of HC length / total midline length
I
DCC expression (% of control)
CCx
IZ
J
Middle
Control r = 0.2765
Dcc cKO r = -0.875
Ratio CC size / total midline length
Ratio IHF length / total midline length
K
Control r = 0.3491
Dcc cKO r = -0.8254
Ratio HC size / total midline length
L
E15 Dcc flox/flox /Tdtomato flox_stop /Emx1 iCre
Control
Emx1 Dcc cKO
DCC
Horizontal
M
GAP43/TDT
100μm
N
GAP43 inset
50μm
O
Mean DCC fluorescence intensity
E15
CCx
MZG
P
Mean GAP43 fluorescence intensity
Q
E15 Emx1: Dcc cKO
TDT Single Z plane
Horizontal
GLAST/TDT
MZG
3V
50μm
R
GLAST-positive/TDTOMATO-positive MZG cell bodies

Figure 6: Conditional knockdown of DCC within EMX1 cells causes a spectrum of callosal phenotypes

(A) Axonal marker TUBB3 (green), (B) TDT (white) or (C) DCC (white) in P0 *Dcc* cKO demonstrate a spectrum of callosal and IHF remodelling phenotypes and a reduction in DCC expression within mice expressing *Emx1^{iCre}*. The CC or CC remnant (CCR) and HC are indicated with white brackets or white arrowheads, and the IHF is indicated with yellow brackets. Red arrowheads indicate axon bundles that have not crossed the midline.

(D) Schema of measurements taken for quantification shown in C-E.

(E) Quantification of the ratio of IHF length normalised to total telencephalic midline length measured for P0 *Dcc* cKO mice.

(F and G) Quantification of CC length (F) and depth (G) normalised to the total telencephalic midline length in P0 *Dcc* cKO mice.

(H) Quantification of HC length normalised to the total telencephalic midline length in P0 *Dcc* cKO mice.

(I) Quantification of DCC expression measured from the cingulate cortex (CCx) and intermediate zone (IZ) of *Dcc* cKO mice.

(J and K) Scatterplots of the relationship between CC length (J) or HC length (K) normalised to total telencephalic midline length and IHF length normalised to total telencephalic midline length for middle horizontal sections of P0 *Dcc* cKO mice. Pearson r correlations are shown.

(L) DCC (white), (M and N) axonal marker GAP43 (green or white, insets) and TDT (magenta) in E15 *Dcc* cKO mice, with quantification of mean DCC fluorescence in (O), and quantification of mean GAP43 fluorescence within 50 µm from the IHF (dotted red lines) in (P) .

(Q) TDT (white or magenta) and glial marker GLAST (green) in E15 *Dcc* cKO with insets and yellow arrowheads indicating GLAST-positive/TDT-positive MZG, and quantified in R.

All graphs represent mean ± SEM. Statistics by Mann-Whitney test or unpaired t test: *p < 0.05, **p < 0.01, ***p < 0.001, ****p < 0.0001, n.s = not significant. See related Figure 5-figure supplement 1 and Supplementary File 1.

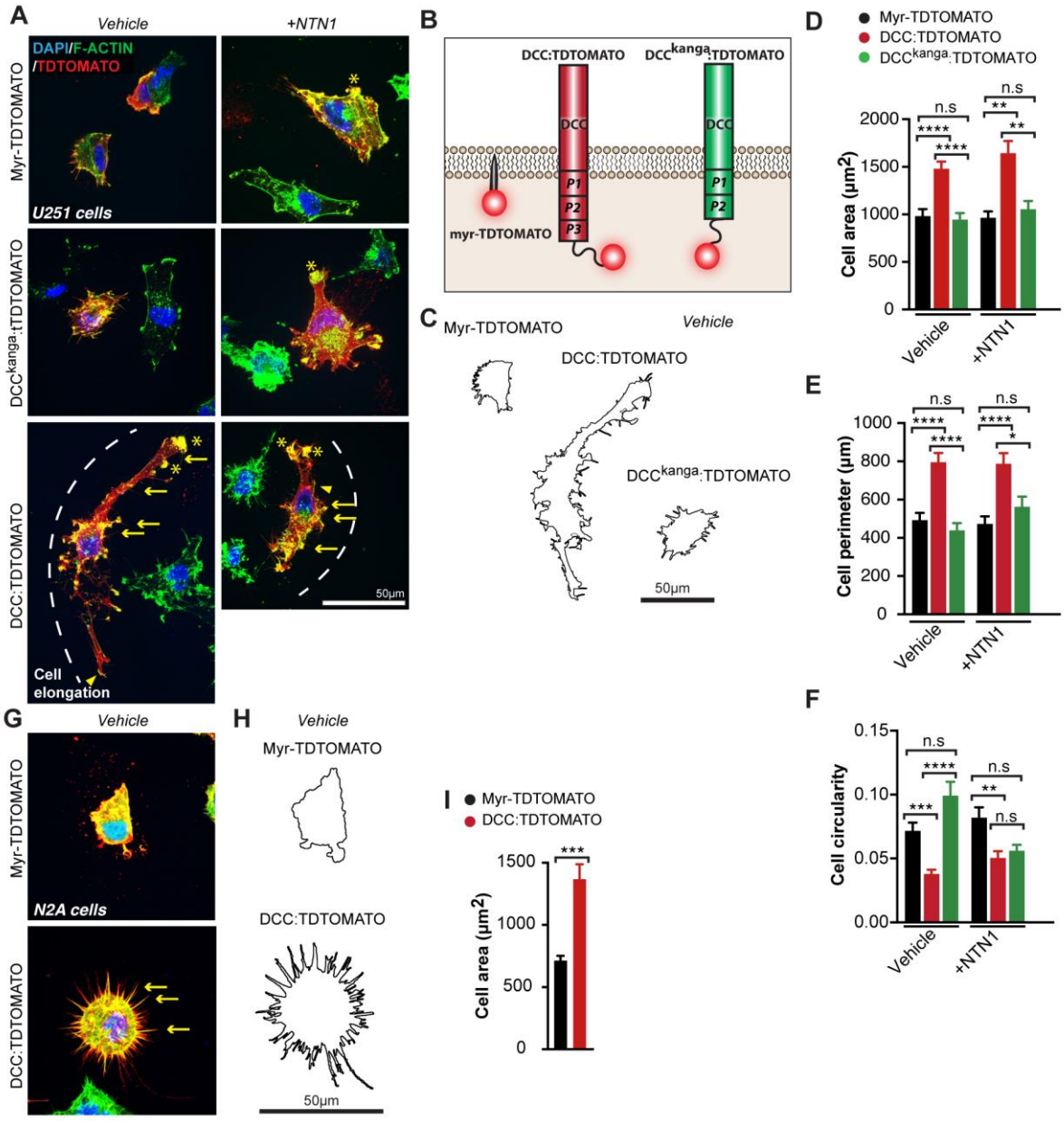

Figure 7: NTN1-DCC signalling promotes cytoskeletal remodelling of astroglia

(A, G) Representative images of U251 glioblastoma cells (A) and N2A cells (G) immunolabelled for TDTOMATO (red), and F-actin (green) following transfection with plasmids encoding Myr-TDTOMATO, DCC:TDTOMATO, or DCC^{kanga}:TDTOMATO demonstrating the presence of actin-rich regions resembling filopodia (yellow arrows), lamellipodia (yellow arrowheads) and membrane ruffles (yellow asterisks) with/without stimulation with recombinant mouse NTN1 protein.

(B) Schema of predicted structure of proteins on the cell membrane encoded by the plasmids expressed in cells from A and G.

(C and H) Outline of cell perimeter generated from images in A and G respectively.

(D-F and I) Quantification of the area, perimeter and circularity of cells represented in A and G. Graphs represent mean ± SEM. Statistics by Kruskal-Wallis test for multiple comparisons: n.s = not significant, *p < 0.05, **p < 0.01, ***p < 0.001, ****p<0.0001. See related Figure 6-figure supplement 1 and Supplementary File 1.

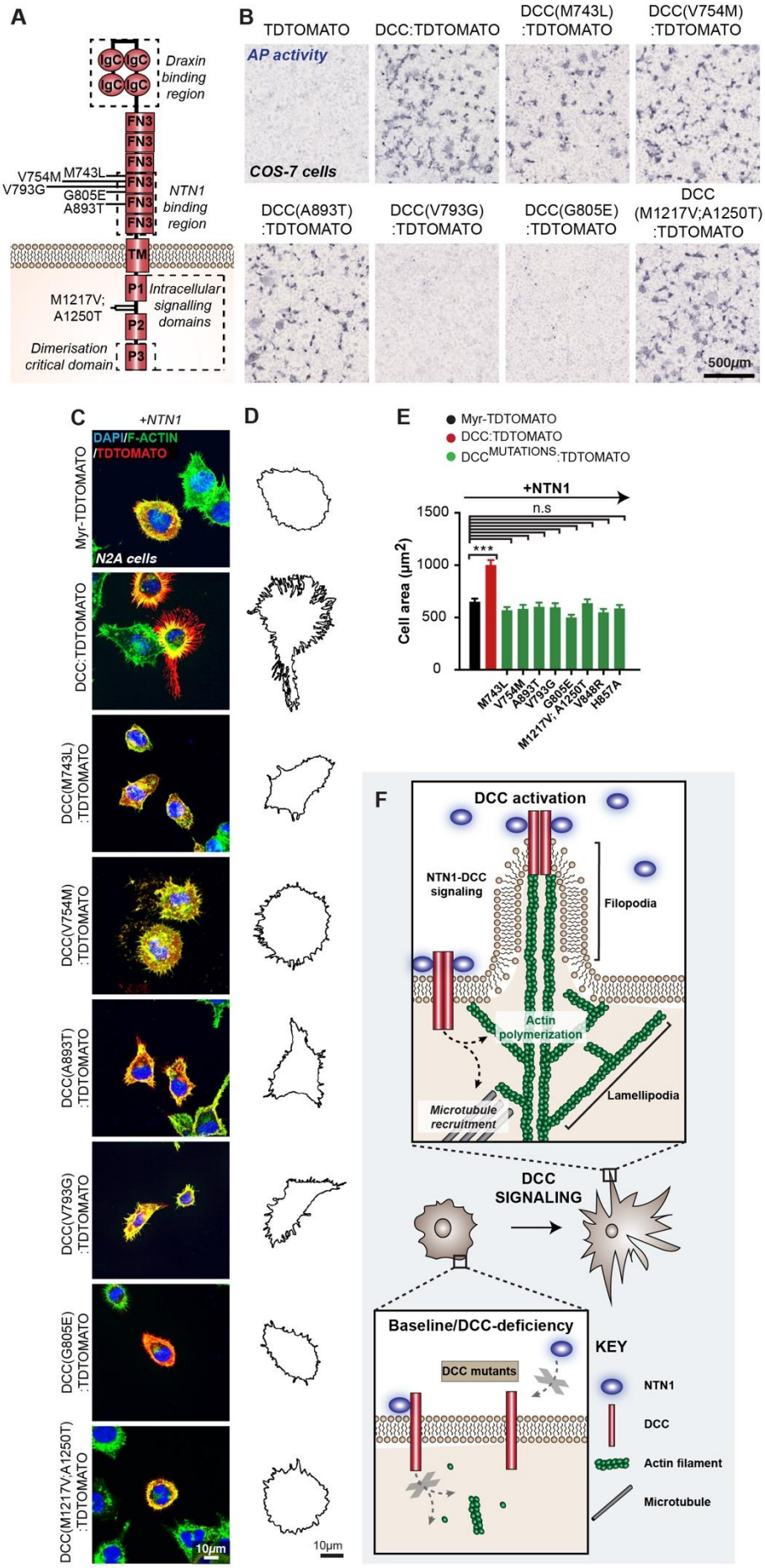
A
IgC
Draxin binding region
FN3
V754M
M743L
V793G
G805E
A893T
NTN1 binding region
TM
P1
M1217V; A1250T
P2
Intracellular signalling domains
Dimerisation critical domain
P3
B
TDTOMATO
DCC:TDTOMATO
DCC(M743L) :TDTOMATO
DCC(V754M) :TDTOMATO
AP activity
COS-7 cells
DCC(A893T) :TDTOMATO
DCC(V793G) :TDTOMATO
DCC(G805E) :TDTOMATO
DCC (M1217V;A1250T) :TDTOMATO
500μm
C
+NTN1
DAPI/F-ACTIN /TDTOMATO
N2A cells
Myr-TDTOMATO
DCC:TDTOMATO
DCC(M743L) :TDTOMATO
DCC(V754M) :TDTOMATO
DCC(A893T) :TDTOMATO
DCC(V793G) :TDTOMATO
DCC(G805E) :TDTOMATO
DCC(M1217V;A1250T) :TDTOMATO
10μm
D
10μm
E
Myr-TDTOMATO
DCC:TDTOMATO
DCC MUTATIONS :TDTOMATO
+NTN1
n.s
***
Cell area (μm2)
1500
1000
500
0
M743L
V754M
A893T
V793G
G805E
M1217V; A1250T
V848R
H857A
F
DCC activation
NTN1-DCC signaling
Filopodia
Actin polymerization
Lamellipodia
Microtubule recruitment
DCC SIGNALING
Baseline/DCC-deficiency
DCC mutants
KEY
NTN1
DCC
Actin filament
Microtubule

Figure 8: *DCC* mutations associated with human callosal agenesis are unable to modulate cell shape and show varied NTN1 binding

(A) Schema of transmembrane receptor DCC and its structural domains. Lines indicate the position of altered residues from missense *DCC* pathogenic variants identified in human individuals with CC abnormalities. FN3 = fibronectin type III-like domain, IgC = immunoglobulin-like type C domain, TM = transmembrane domain, P = P motif.

(B) Colourimetric detection of alkaline phosphatase activity in COS-7 cells transfected with plasmids encoding TDTOMATO, DCC:TDTOMATO, and mutant DCC:TDTOMATO constructs, and incubated with a NTN1 alkaline phosphatase fusion protein.

(C) Representative images of N2A cells immunolabelled for TDTOMATO (red), and F-actin (green) following transfection with plasmids encoding Myr-TDTOMATO, DCC:TDTOMATO, or DCC:TDTOMATO carrying missense mutations and stimulated with recombinant mouse NTN1 protein.

(D) Outline of cell perimeter generated from images in B.

(E) Quantification of the area of cells represented in B. Graph represents mean ± SEM. Statistics by Kruskal-Wallis test for multiple comparisons: n.s = not significant, ***$p < 0.001$.

(F) Schema of model for DCC-mediated changes in cell shape: Activation of DCC by NTN1 induces dimerisation of the receptor and recruits intracellular signaling effectors to regulate actin polymerisation for filopodia and lamellipodia formation, and to regulate microtubule dynamics to promote membrane protrusions. Mutations that affect DCC signalling prevent DCC-mediated changes in cell shape.

See related Figure 6-figure supplement 1 and Supplementary File 1.

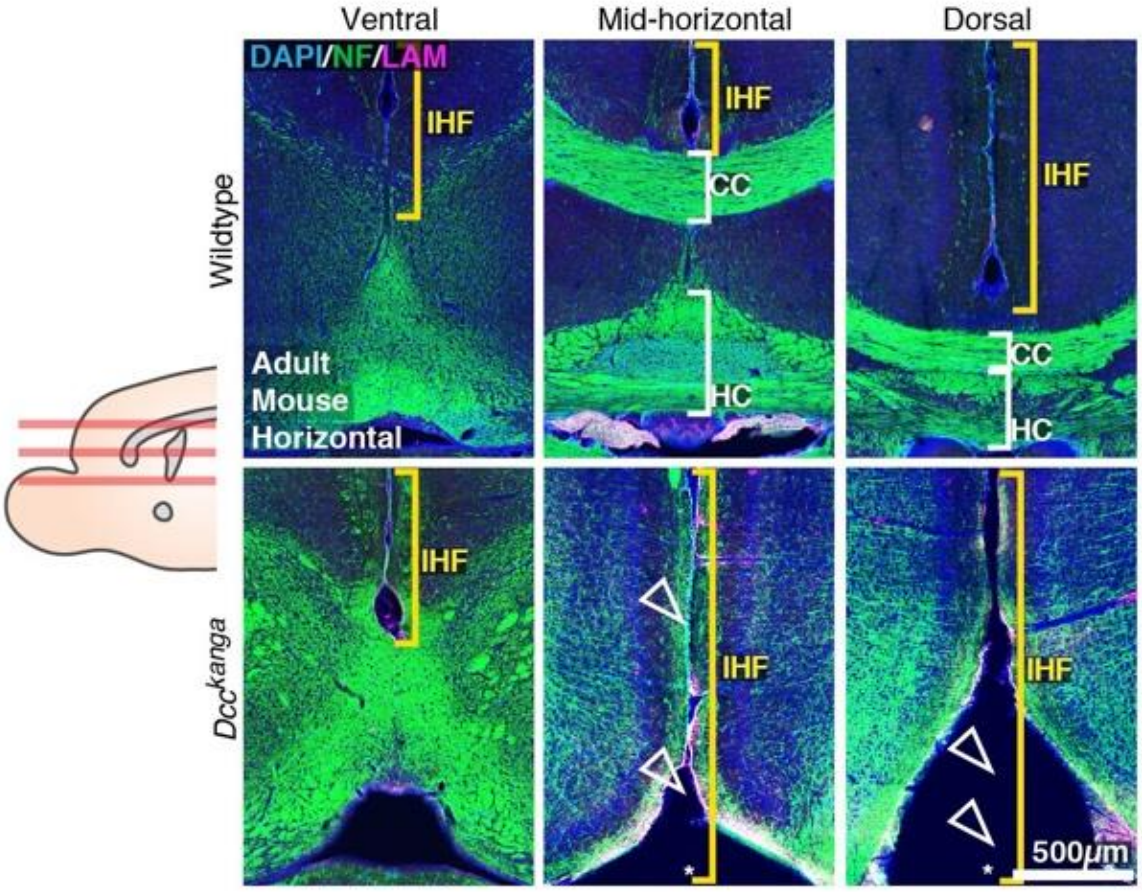

Figure 1-figure supplement 1: The IHF is not remodelled in adult *Dcc*^{kanga} mice

Neurofilament (NF)-positive axons (green) and pan-Laminin (LAM)-positive leptomeninges and basement membrane (magenta) in adult wildtype and *Dcc*^{kanga} mice reveal presence/absence of the CC and HC (white brackets and arrowheads), the extent of the IHF (yellow brackets) and absence of the septal substrate in *Dcc*^{kanga} mice (asterisks).

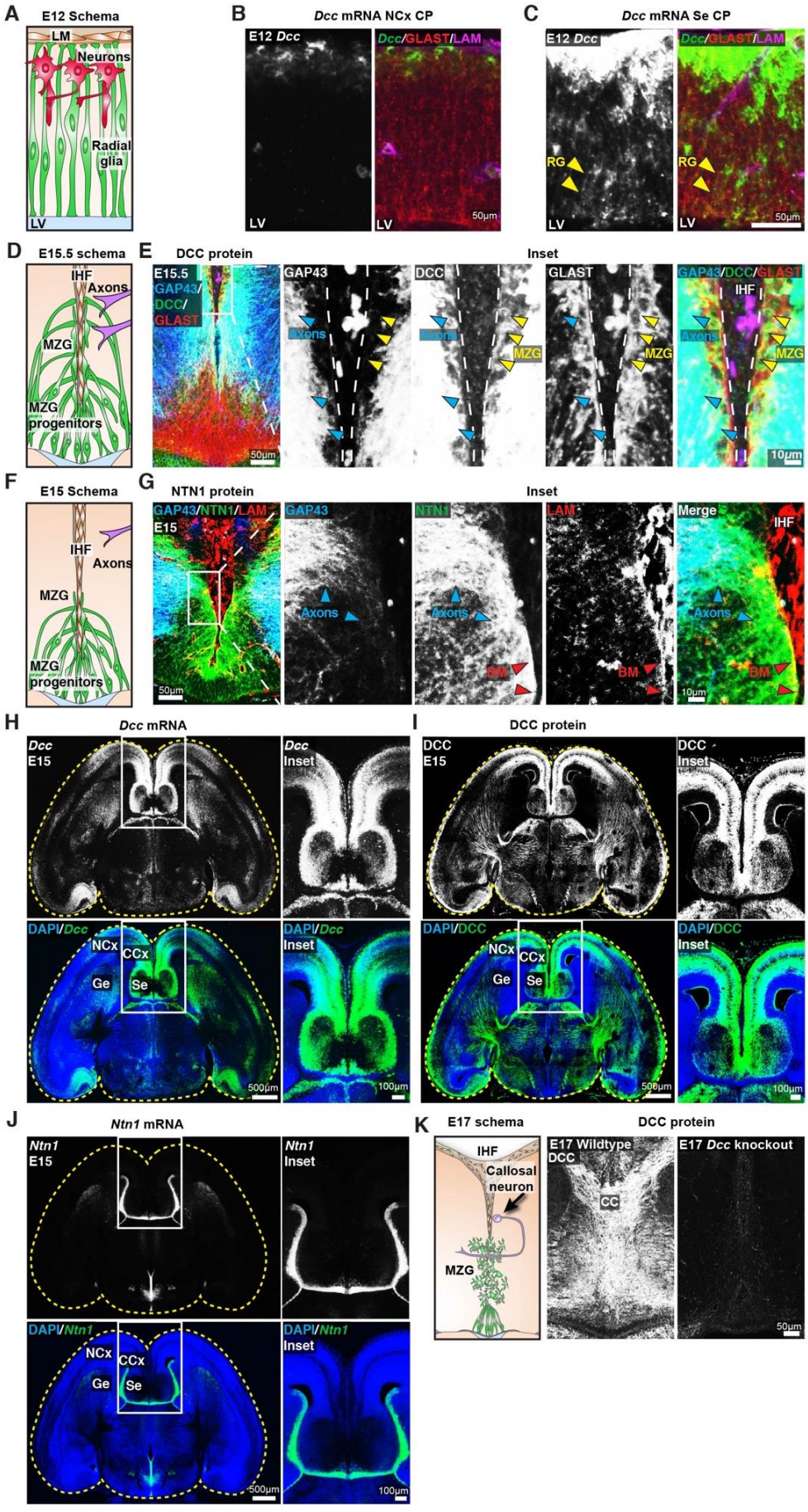
A
E12 Schema
LM
Neurons
Radial glia
LV
B
Dcc mRNA NCx CP
E12 Dcc
Dcc/GLAST/LAM
LV
50μm
C
Dcc mRNA Se CP
RG
D
E15.5 schema
IHF
Axons
MZG
MZG progenitors
E
DCC protein
Inset
E15.5 GAP43/ DCC/ GLAST
GAP43
DCC
GLAST
GAP43/DCC/GLAST
10μm
F
E15 Schema
G
NTN1 protein
GAP43/NTN1/LAM
E15
NTN1
LAM
Merge
BM
H
Dcc mRNA
Dcc E15
Dcc Inset
DAPI/Dcc
NCx
CCx
Ge
Se
500μm
100μm
I
DCC protein
DCC E15
DCC Inset
DAPI/DCC
J
Ntn1 mRNA
Ntn1 E15
Ntn1 Inset
DAPI/Ntn1
K
E17 schema
Callosal neuron
E17 Wildtype DCC
CC
E17 Dcc knockout

1455

Figure 2-figure supplement 1: DCC is expressed in MZG

(A, D and F) Schemas of key cellular components within the telencephalic midline.

(B and C) *Dcc* mRNA (green), Glast-positive glia (red), and pan-laminin (LAM)-positive leptomeninges and basement membrane (magenta) across the cortical plate (Cp) within the neocortex (NCx) or septum (Se) in horizontal sections of wildtype mice reveals *Dcc*-positive/Glast-positive radial glial (RG) fibers (yellow arrowheads). LV = lateral ventricle.

(E) DCC protein (green), Gap43-positive axons (blue), and Glast-positive MZG (red) in horizontal sections of E15 wildtype mice (right panels), indicate DCC-positive/Glast-positive cells (yellow arrowheads) and DCC-positive/Gap43-positive axons (blue arrowheads) that are approaching the midline and are adjacent to MZG.

(G) Gap43-positive axons (blue), NTN1 protein (green), and pan-Laminin (LAM)-positive leptomeninges and basement membrane (red) in horizontal sections of E15 wildtype mice reveal NTN1-positive/Gap43-positive axons (blue arrowheads) approaching the midline and NTN1-positive/LAM-positive basement membrane (BM; red arrowheads) of the IHF.

(H, I and J) Mid-horizontal tissue sections encompassing the entire telencephalon (yellow outlines) with in situ hybridization for *Dcc* mRNA or *Ntn1* mRNA or immunohistochemistry for DCC protein (all white or green), counterstained with DAPI (blue). Insets of the telencephalic midline are shown on the right.

(K) DCC immunohistochemistry in horizontal sections of E17 wildtype and *Dcc* knockout mice with schema of key cellular components within the telencephalic midline.

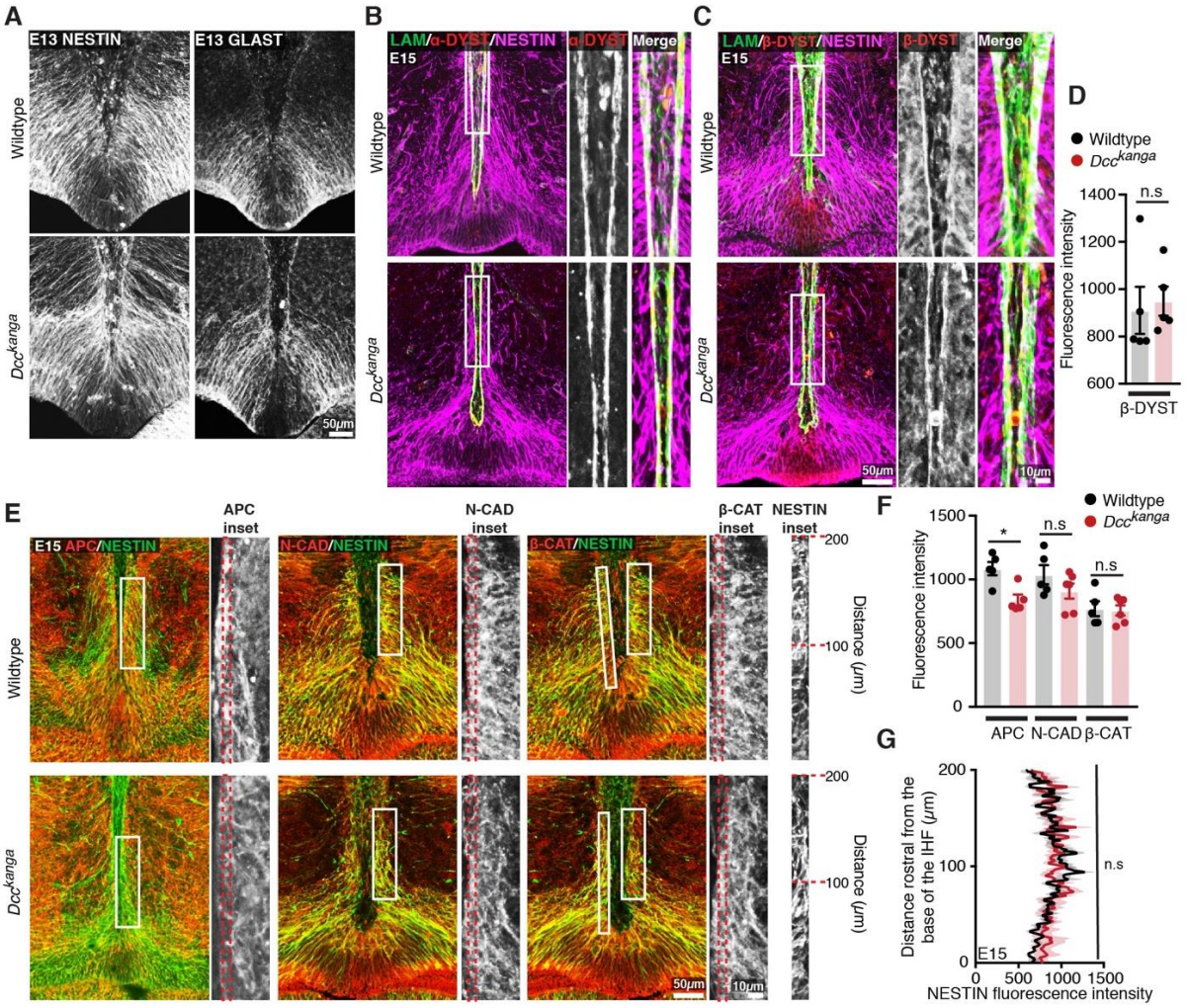

Figure 3-figure supplement 1: DCC is not required for endfeet attachment or molecular polarity of MZG

(A) Nestin-positive radial glia (white), and Glast-positive MZG (white) in horizontal sections of E13 wildtype and *Dcc*^{kanga} mice.

(B and C) Pan-Laminin (LAM)-positive leptomeninges and basement membrane (green), Nestin-positive radial glia (magenta), and α-dystroglycan (α-DYST; red; B), or β-dystroglycan (β-DYST; red, C) in horizontal sections of E15 wildtype and *Dcc*^{kanga} mice.

(D) Quantification of fluorescence intensity of β-DYST along 200 μm of the IHF surface as outlined with red dotted box in C.

(E) Nestin-positive radial glia (green) with either Adenomatous polyposis coli (APC, red), N-cadherin (N-CAD; red), or β-catenin (β-CAT; red) in horizontal sections of E15 wildtype and *Dcc*^{kanga} mice with insets.

(F) Quantification of the fluorescence intensity of APC, N-CAD and β-CAT within 5 μm of the IHF as outlined in red dotted-edged boxes from E.

(G) Quantification of the fluorescence intensity of Nestin-positive radial glial endfeet within 5 µm of the IHF surface from inset in E.

All graphs represent mean ± SEM. Statistics by Mann-Whitney test: n.s = not significant, *p < 0.05. See related Supplementary File 1.

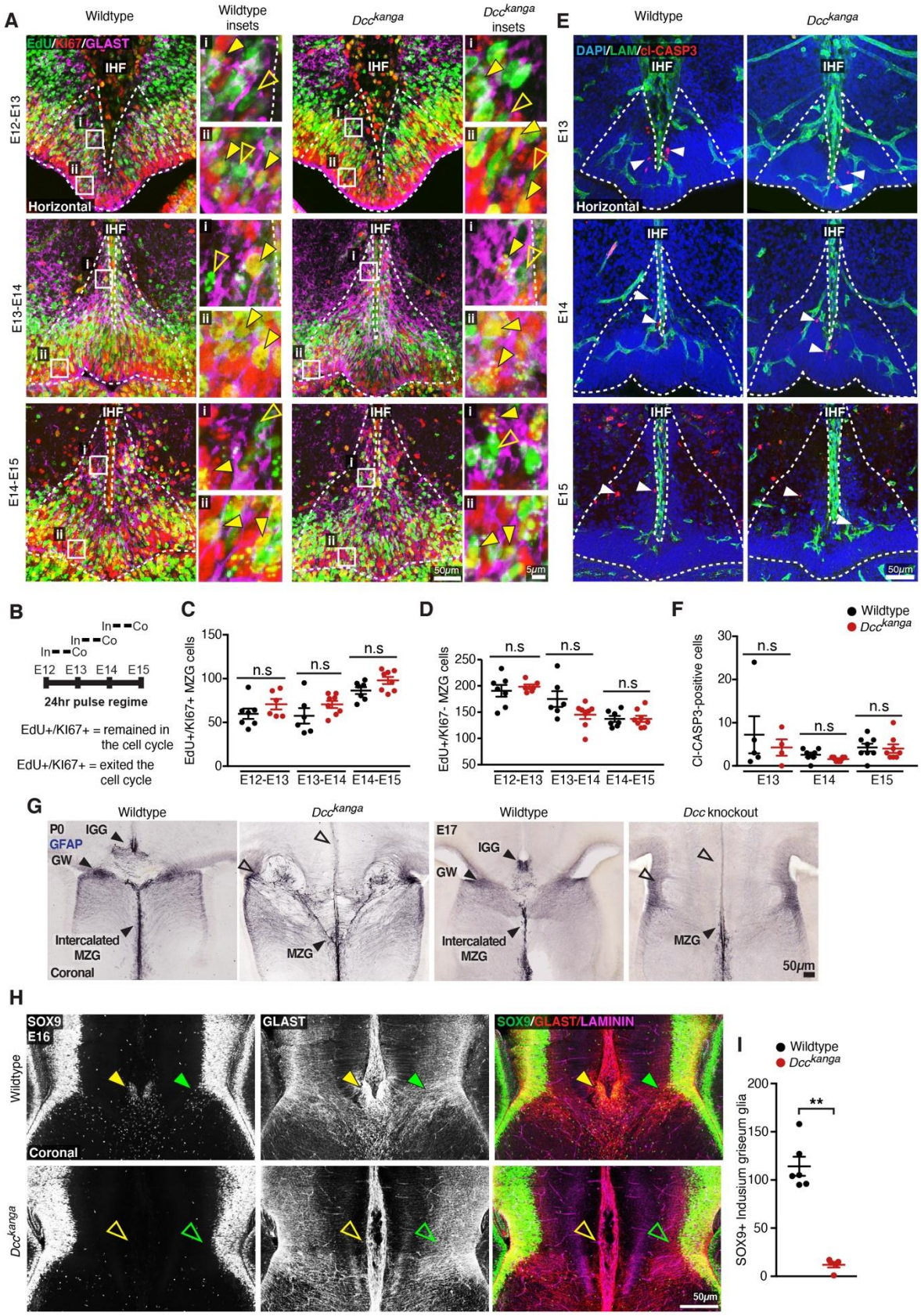
A
Wildtype
Wildtype insets
Dcc^kanga
Dcc^kanga insets
EdU/KI67/GLAST
IHF
Horizontal
E12-E13
E13-E14
E14-E15
50μm
5μm
E
Wildtype
Dcc^kanga
DAPI/LAM/cl-CASP3
E13
E14
E15
B
In
Co
E12 E13 E14 E15
24hr pulse regime
EdU+/KI67+ = remained in the cell cycle
EdU+/KI67+ = exited the cell cycle
C
EdU+/KI67+ MZG cells
n.s
D
EdU+/KI67- MZG cells
F
Wildtype
Dcc^kanga
cl-CASP3-positive cells
G
Wildtype
Dcc^kanga
Wildtype
Dcc knockout
P0
IGG
GFAP
GW
Intercalated MZG
Coronal
MZG
E17
H
SOX9
E16
GLAST
SOX9/GLAST/LAMININ
Wildtype
Dcc^kanga
Coronal
I
Wildtype
Dcc^kanga
SOX9+ Indusium griseum glia
**

1501
1502

Figure 4-figure supplement 1: DCC does not regulate the proliferation or cell death of MZG but regulates the formation of the indusium griseum glia and glial wedge

(A) Mouse MZG cells were birth-dated with the thymidine analog EdU every 24 hours, from E12 to E15 in wildtype and *Dcc*^{kanga} mice. Representative images of EdU (green), cell cycle marker, Ki67 (red), and MZG marker Glast (magenta) are shown for wildtype and *Dcc*^{kanga} mice, with the distribution of MZG progenitors within the telencephalic hinge niche outlined with white dotted lines. Yellow arrowheads in insets point out EdU cells that are either Ki57-positive (filled arrowheads) or Ki67-negative (open arrowheads) in selected insets. The number of cells expressing each marker is quantified in (C) and (D).

(B) Schema of the EdU injection (In) and collection (Co) regime and interpretation of co-labelled and non-co-labelled cells.

(E) Laminin(LAM)-positive leptomeninges and basement membrane (green) and cleaved-caspase3-positive apoptotic cells (red, white arrowheads) in E13-E15 wildtype and *Dcc*^{kanga} mice. The number of cleaved-caspase3 (Cl-CASP3)-positive cells within the telencephalic hinge niche (white dotted lines) is quantified in (F).

(G) Mature astroglial marker GFAP in coronal sections of P0 *Dcc*^{kanga} mice and E17 *Dcc* knockout mice and their wildtype littermates reveals midline glial populations, the glial wedge (GW), the indusium griseum glia (IGG), and the MZG (filled arrowheads) or their absence/malformation (open arrowheads).

(H) Glial-specific cell body marker SOX9 (white or green), glial cell membrane marker Glast (white or red), and IHF marker Laminin (magenta) in E16 coronal sections from *Dcc*^{kanga} mice indicate the presence or absence of SOX9-positive/Glast-positive cell bodies at the pial surface of the IHF (yellow arrowheads) and within the intermediate zone (green arrowheads).

(I) Quantification of SOX9-positive IGG cell bodies at the pial surface of the IHF in E16 wildtype and *Dcc*^{kanga} mice from immunohistochemistry in G.

All graphs represent mean ± SEM. Statistics by Mann-Whitney test: n.s = not significant, **p < 0.01. See related Supplementary File 1.

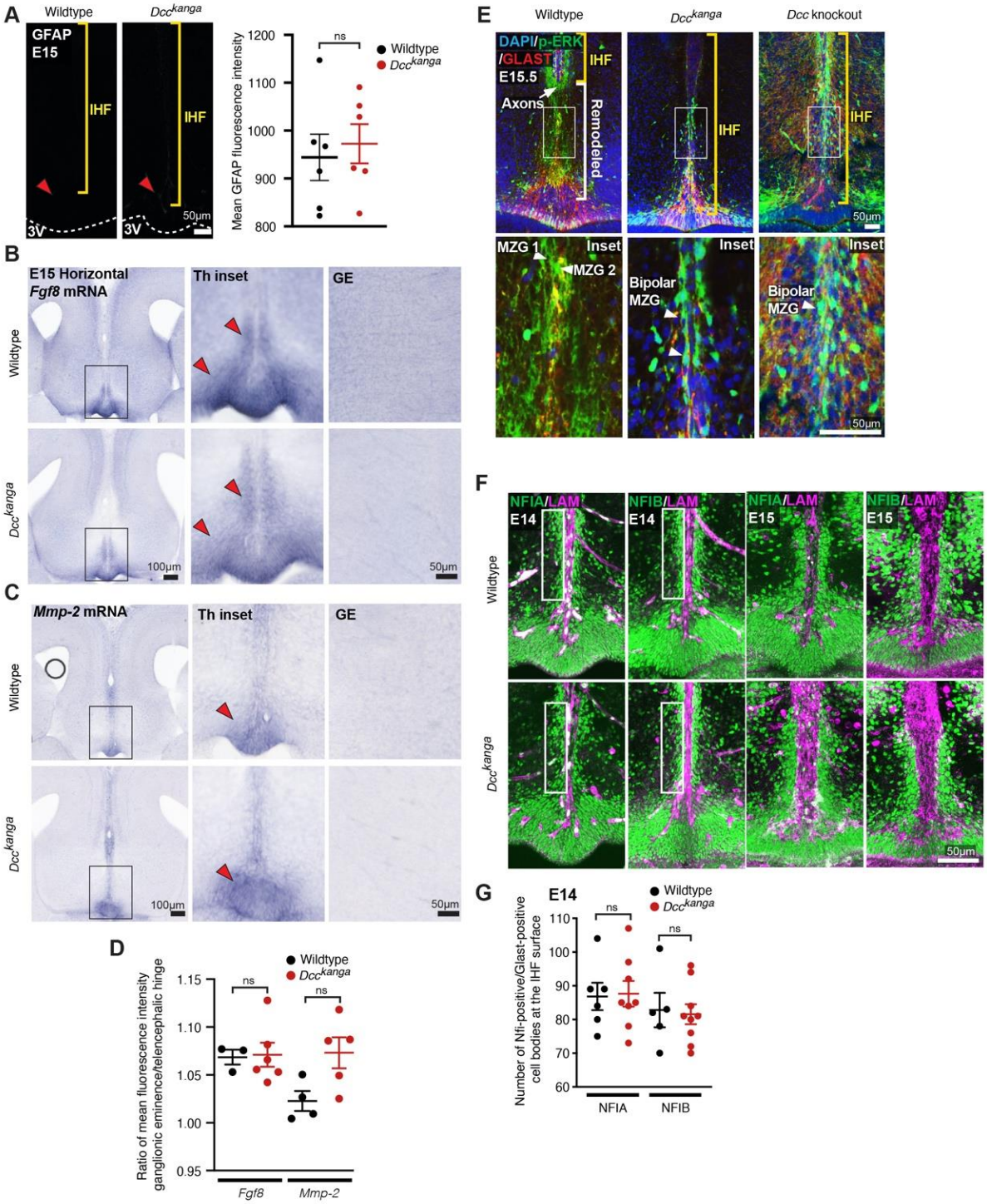

Figure 5-figure supplement 1: DCC is not required for astroglial differentiation of MZG

(A) Mature astroglial marker Gfap (white) in horizontal sections of E15 wildtype and *Dcc*^{kanga} mice with quantification of Gfap average fluorescence intensity. The surface of the third ventricle (3V) is outlined with dotted white lines. Red arrowheads indicate

reactive blood vessels that are not Gfap-positive glia. Yellow brackets indicate the position of the interhemispheric fissure (IHF).

Fgf8 mRNA (B) or *Mmp-2* mRNA (C) in horizontal sections of E15 wildtype and *Dcc*^{kanga} mice. Red arrowheads indicate reactivity in the telencephalic hinge (Th) in insets, right. A region of the ganglionic eminence (GE) where Fgf8 is not expressed is shown and was used to normalise specific Fgf8 expression within the Th with background immunoreactivity as quantified in D.

(E) Phosphorylated p44/42 Mapk or Erk1/2 (p-ERK, green), and Glast-positive MZG (red) in horizontal sections of E15.5 wildtype, *Dcc*^{kanga} mice and *Dcc* knockout mice reveal extent of IHF (yellow brackets) and remodelled regions of the septum (white brackets) with p-ERK-positive MZG in insets.

(F) Nuclear factor I (NFI) A or B (green), and pan-Laminin (LAM)-positive leptomeninges and basement membrane (magenta) in horizontal sections of E14 and E15 wildtype and *Dcc*^{kanga} mice. NFI-positive/Glast-positive MZG cell bodies at the IHF surface are outlined with white boxes and quantified in G. Data is represented as mean ± SEM. Significant differences were determined with non-parametric Mann-Whitney tests. ns = not significant, Hi = telencephalic hinge. LAM = laminin

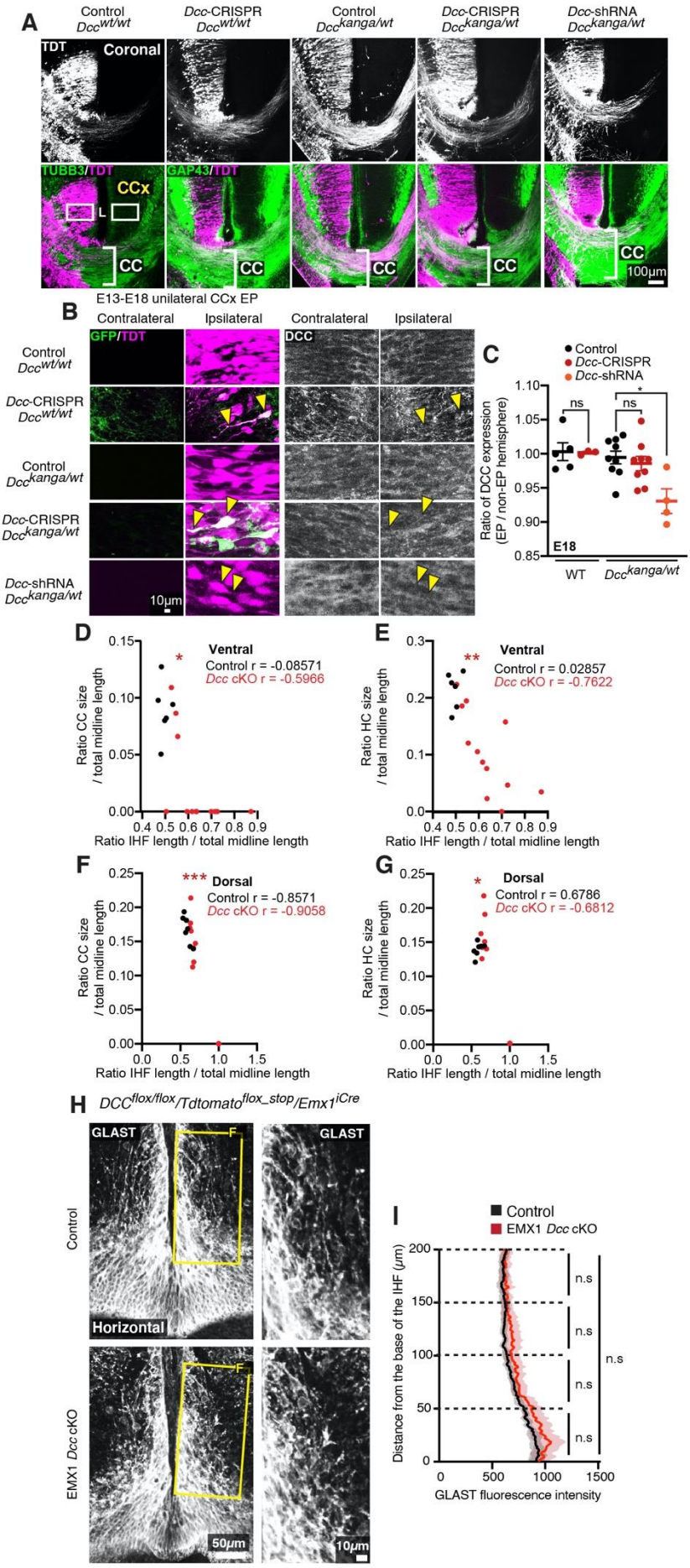

Figure 6-figure supplement 1: *Dcc* knockdown via targeted in utero electroporation does not cause CC abnormalities.

(A) TUBB3 (green) and TDT (white or magenta) in E18 *Dcc*^{kanga} mice electroporated with pCAG-TDTOMATO and either *Dcc*-CRISPR or *Dcc*-shRNA constructs into the CCx at E13. The CC is outlined with white brackets and white boxes indicate the location of panels represented in B.

(B) GFP (green), TDT (magenta) or DCC (white) in E18 *Dcc*^{kanga} mice electroporated with pCAG-TDTOMATO and either *Dcc*-CRISPR or *Dcc*-shRNA constructs into the CCx at E13. GFP indicates expression of the *Dcc*-CRISPR and yellow arrowheads indicate the

location of select electroporated cells.
(C) Quantification of the ratio of DCC expression between ipsilateral (electroporated; EP) and contralateral (non-electroporated) hemispheres shown in B.
(D-G) Scatterplots of the relationship between CC length or HC length normalised to total telencephalic midline length and IHF length normalised to total telencephalic midline length for ventral and dorsal horizontal sections of P0 *Dcc* cKO mice. Nonparametric Spearman r correlations are shown.
(H) Glial marker GLAST (white), in E15 *Dcc* cKO mice demonstrates the distribution of GLAST-positive MZG. Yellow boxes indicate region shown in insets, right and quantified in E.
(I) Quantification of mean GLAST fluorescence within the telencephalic hinge from insets in D.

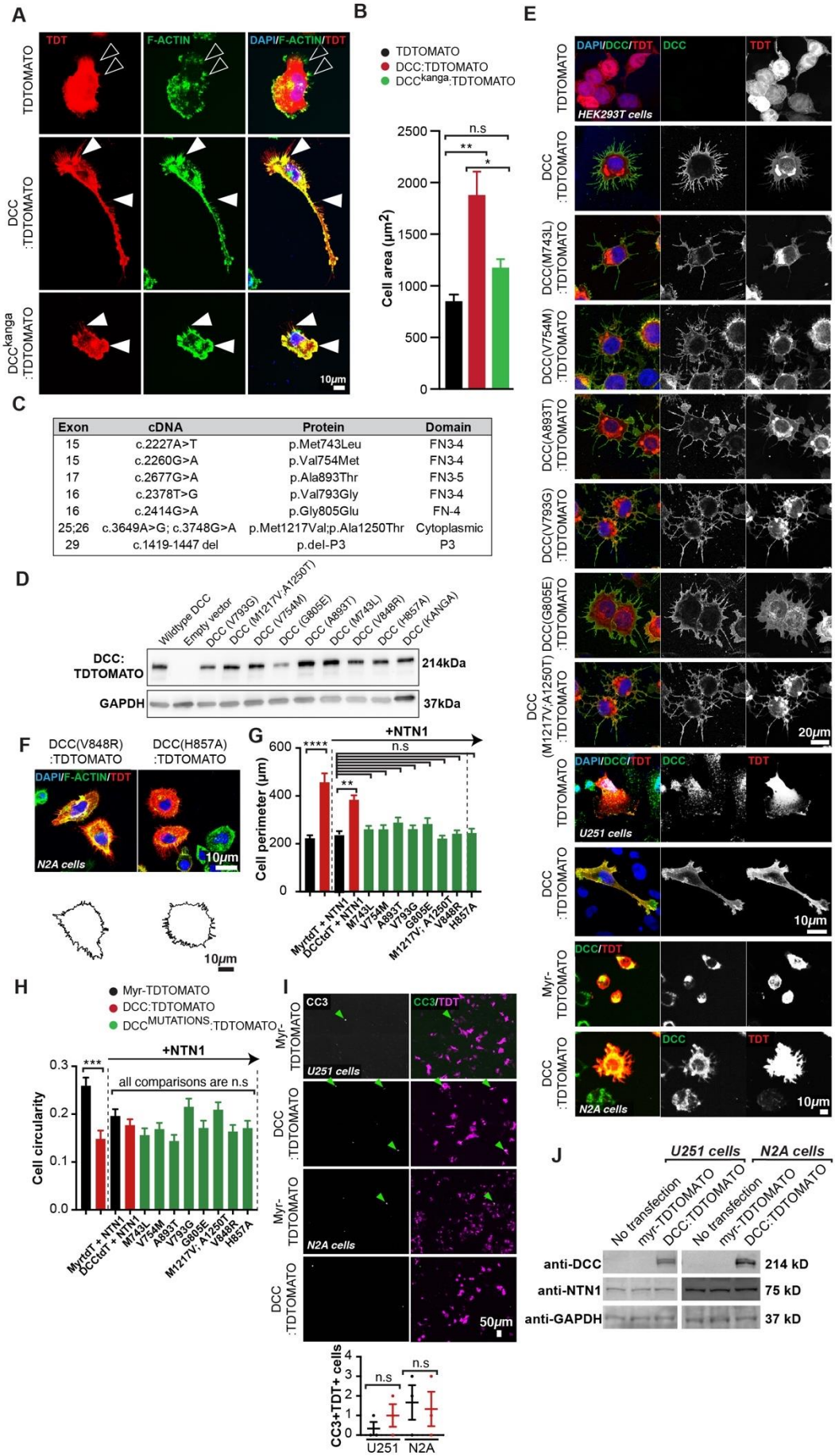
A
TDT
F-ACTIN
DAPI/F-ACTIN/TDT
TDTOMATO
DCC :TDTOMATO
DCC^kanga :TDTOMATO
10μm
B
TDTOMATO
DCC:TDTOMATO
DCC^kanga:TDTOMATO
Cell area (μm²)
n.s
**
*
C
Exon | cDNA | Protein | Domain
15 | c.2227A>T | p.Met743Leu | FN3-4
15 | c.2260G>A | p.Val754Met | FN3-4
17 | c.2677G>A | p.Ala893Thr | FN3-5
16 | c.2378T>G | p.Val793Gly | FN3-4
16 | c.2414G>A | p.Gly805Glu | FN-4
25;26 | c.3649A>G; c.3748G>A | p.Met1217Val;p.Ala1250Thr | Cytoplasmic
29 | c.1419-1447 del | p.del-P3 | P3
D
Wildtype DCC
Empty vector
DCC (V793G)
DCC (M1217V;A1250T)
DCC (V754M)
DCC (G805E)
DCC (A893T)
DCC (M743L)
DCC (V848R)
DCC (H857A)
DCC (KANGA)
DCC: TDTOMATO
214kDa
GAPDH
37kDa
E
DAPI/DCC/TDT
DCC
TDT
HEK293T cells
DCC(M743L) :TDTOMATO
DCC(V754M) :TDTOMATO
DCC(A893T) :TDTOMATO
DCC(V793G) :TDTOMATO
DCC(G805E) :TDTOMATO
DCC (M1217V;A1250T) :TDTOMATO
20μm
U251 cells
N2A cells
10μm
Myr-TDTOMATO
DCC/TDT
F
DCC(V848R) :TDTOMATO
DCC(H857A) :TDTOMATO
DAPI/F-ACTIN/TDT
N2A cells
10μm
G
+NTN1
n.s
****
**
Cell perimeter (μm)
MyrtdT + NTN1
DCCtdT + NTN1
M743L
V754M
A893T
V793G
G805E
M1217V; A1250T
V848R
H857A
H
Myr-TDTOMATO
DCC:TDTOMATO
DCC^MUTATIONS:TDTOMATO
+NTN1
***
all comparisons are n.s
Cell circularity
I
CC3
CC3/TDT
U251 cells
N2A cells
50μm
CC3+TDT+ cells
n.s
U251
N2A
J
U251 cells
N2A cells
No transfection
myr-TDTOMATO
DCC:TDTOMATO
anti-DCC
anti-NTN1
anti-GAPDH
214 kD
75 kD
37 kD

Figure 7-figure supplement 1: Mutant *DCC* receptors are expressed and trafficked normally but are unable to modulate cell shape

(A) Representative images of U251 glioblastoma cells immunolabelled for TDTOMATO (red), and F-actin (green) following transfection with plasmids encoding TDTOMATO, DCC:TDTOMATO, or DCC^{kanga}:TDTOMATO demonstrating predominant presence or absence of colocalised TDTOMATO with F-actin (arrowheads).

(B) Quantification of average cell area from U251 cells represented in A.

(C) Specific missense mutations were introduced into mouse pCAG-DCC:TDTOMATO and exon 29 was removed (del = deleted) to create the DCC^{kanga}:TDTOMATO construct.

(D) COS-7 cells were transfected with pCAG-DCC:TDTOMATO constructs, including those carrying specific point mutations and the DCC^{kanga}:TDTOMATO construct. After 48 hours, cells were lysed, and a western blot was performed for mouse DCC and GADPH. Specific bands at 214kD and 37kD are shown.

(E) HEK293T, N2A and U251 cells were transfected with pCAG-DCC:TDTOMATO constructs, including those carrying specific point mutations. After 24 hours, cells were fixed and immunohistochemistry was performed for the N-terminal of DCC without permeabilisation to detect membrane-inserted DCC (HEK293T) or for the C-terminal of DCC with permeabilisation (N2A and U251 cells).

(F) Representative images of N2A cells immunolabelled for TDTOMATO (red), and F-actin (green) following transfection with plasmids encoding DCC:TDTOMATO carrying missense mutations and stimulated with recombinant mouse NTN1 protein with cell perimeter outlined below. The cell perimeter and cell circularity of these cells, and those represented in Figure 7B are quantified in (G) and (H) respectively.

(I) Representative images of U251 and N2A cells immunolabelled for TDTOMATO (magenta), and cleaved-caspase3 (CC3; green) following transfection with plasmids encoding DCC:TDTOMATO and myr-TDTOMATO. Arrowheads indicate TDTOMATO-positive/CC3-positive cells, which are quantified below.

(J) U251 and N2A cells were transfected with plasmids encoding myr-TDTOMATO and DCC:TDTOMATO or not transfected. After 20 hours, cells were lysed, and a western blot was performed for mouse DCC, NTN1 and GADPH. Specific bands at 214kD, 75kD and 37kD are shown from n = 3 biological replicates.

All graphs represent mean ± SEM. Statistics by Kruskal-Wallis test for multiple comparisons: n.s = not significant with p > 0.05, *p < 0.05, **p < 0.01, ***p < 0.001, ****p < 0.0001. See related Figure 6, Figure 7 and Supplementary File 1.

All graphs represent mean ± SEM. Statistics by Mann-Whitney test or unpaired t test: *p < 0.05, n.s = not significant with p > 0.05. See related Figure 7, Figure 8 and Supplementary File 1.

Figure 1-source data 1: Ratio of IHF length / total telencephalic midline length in *Dcc* and *Ntn1* mouse mutants

Figure 3-source data 1: Fluorescence intensity of GLAST and ratio of glial distribution / total midline length in *Dcc* mouse mutants

Figure 4-source data 1: Number and distribution of SOX9-positive MZG in *Dcc* mouse mutants

Figure 5-source data 1: Normalised fluorescence intensity of GFAP adjacent to the telencephalic midline in E17 *Dcc* and *Ntn1* mutant mice

Figure 6-source data 1: Measurements of IHF, CC and HC length and depth, DCC fluorescence and GLAST-positive/TDTOMATO-positive MZG cell bodies in *Dcc* cKO mice

Figure 7-source data 1: U251 or N2A cell area, perimeter and circularity following overexpression of DCC:TDTOMATO or myr-TDTOMATO

Figure 8-source data 1: N2A cell area following overexpression of DCC:TDTOMATO, DCC:TDTOMATO carrying a mutation or myr-TDTOMATO

Figure 3-figure supplement 1-source data 1: Fluorescence intensity of β-DYST, β-CAT, APC and N-CAD along the IHF surface in Dcc^{kanga} mice

Figure 4-figure supplement 1-source data 1: Number of cells expressing EdU and Ki67, Cleaved-caspase 3 and SOX9 along the IHF surface in Dcc^{kanga} mice

Figure 5-figure supplement 1-source data 1: Fluorescence intensity measurements for GFAP, *Fgf8* and *Mmp-2* mRNA, and quantification of NFI-positive/GLAST-positive cell bodies in *Dcc*^{kanga} mice

Figure 6-figure supplement 1-source data 1: Quantification of the ratio of DCC expression between hemispheres, measurements of IHF length, CC length and HC length, and GLAST fluorescence intensity along the IHF surface in *Dcc cKO* mice

Figure 7-figure supplement 1-source data 1: U251 cell area, N2A cell perimeter and circularity and cleaved-caspase3 expression following overexpression of DCC:TDTOMATO, DCC:TDTOMATO carrying a mutation, Myr-TDTOMATO, or TDTOMATO alone.

Supplementary file 1: Statistics

Statistics related to quantified data in figures 1-8 and figure 1-7 supplements. CA = cell area, CP = cell perimeter, CC3 = cleaved-caspase 3DCCK = DCCKanga, E = embryonic day, EP = electroporated, exp = experimental, FI = fluorescence intensity, IGG = indusium griseum glia, MZG = midline zipper glia, P = postnatal day, ROI = region of interest, TDT = TDTOMATO, vs. = versus, wt = wildtype.

Supplementary file 2: Key resources table

Resources used to generate the data contained within figures 1-8 and figure 1-7 supplements. See materials and methods for further details.